A domain decomposition method for solving the three-dimensional time-harmonic Maxwell equations discretized by discontinuous Galerkin methods

Victorita Dolean, Stephane Lanteri, Ronan Perrussel

INRIA

INSTITUT NATIONAL DE RECHERCHE EN INFORMATIQUE ET EN AUTOMATIQUE

Une méthode de décomposition de domaine pour la résolution numérique des équations de Maxwell tridimensionnelles en domaine harmonique discrétisées par des méthodes de type Galerkin discontinu

Victorita Dolean — Stéphane Lanteri — Ronan Perrussel

N° 6220

Juin 2007

Thème NUM

ISSN 0249-6399 ISRN INRIA/RR--6220--FR+ENG

Une méthode de décomposition de domaine pour la résolution numérique des équations de Maxwell tridimensionnelles en domaine harmonique discrétisées par des méthodes de type Galerkin discontinu

Victorita Dolean * , Stéphane Lanteri † , Ronan Perrussel ‡

Thème NUM — Systèmes numériques
Projet Caiman

Rapport de recherche n° 6220 — Juin 2007 — 39 pages

Résumé : Nous présentons ici une méthode de décomposition de domaine pour la résolution des équations de Maxwell tridimensionnelles en domaine harmonique discrétisées par une méthode Galerkin discontinu. Pour permettre le traitement de géométries irrégulières, la méthode Galerkin discontinu est formulée en maillages tétraédriques non-structurés. La stratégie de résolution par décomposition de domaine consiste en un algorithme de type Schwarz où des conditions absorbantes du premier ordre sont imposées aux interfaces entre sous-domaines voisins. Un solveur direct creux multifrontal est utilisé pour la résolution des problèmes locaux posés dans chaque sous-domaine. La méthode de décomposition de domaine résultante peut s'interpréter comme un solveur hybride itératif/direct pour les systèmes algébriques creux à coefficients complexes résultant de la discrétisation des équations de Maxwell en domaine harmonique par des méthodes de type Galerkin discontinu.

Mots-clés : électromagnétisme numérique, équations de Maxwell en domaine harmonique, méthode Galerkin discontinu, maillages non-structurés, méthode de décomposition de domaine, algorithme de Schwarz.

* Université de Nice-Sophia Antipolis Laboratoire J.A. Dieudonné, CNRS UMR 6621 06108 Nice Cedex, France
† INRIA, 2004 Route des Lucioles, BP 93 06902 Sophia Antipolis Cedex, France
‡ École Centrale de Lyon Laboratoire Ampère, CNRS UMR 5005 69134 Écully Cedex, France

Unité de recherche INRIA Sophia Antipolis
2004, route des Lucioles, BP 93, 06902 Sophia Antipolis Cedex (France)
Téléphone : +33 4 92 38 77 77 — Télécopie : +33 4 92 38 77 65

A domain decomposition method for solving the three-dimensional time-harmonic Maxwell equations discretized by discontinuous Galerkin methods

Abstract: We present here a domain decomposition method for solving the three-dimensional time-harmonic Maxwell equations discretized by a discontinuous Galerkin method. In order to allow the treatment of irregularly shaped geometries, the discontinuous Galerkin method is formulated on unstructured tetrahedral meshes. The domain decomposition strategy takes the form of a Schwarz-type algorithm where a first-order absorbing condition is imposed at the interfaces between neighboring subdomains. A multifrontal sparse direct solver is used at the subdomain level. The resulting domain decomposition strategy can be viewed as a hybrid iterative/direct solution method for the large, sparse and complex coefficients algebraic system resulting from the discretization of the time-harmonic Maxwell equations by a discontinuous Galerkin method.

Key-words: computational electromagnetism, time-harmonic Maxwell's equations, discontinuous Galerkin method, unstructured meshes, domain decomposition method, Schwarz algorithm.

Table des matières

1 Introduction

This work aims at developing a high-performance numerical methodology for the computer simulation of time-harmonic electromagnetic wave propagation problems in irregularly shaped domains and heterogeneous media. In this context, we are naturally led to consider volume discretization methods (*i.e.* finite difference, finite volume or finite element methods) as opposed to surface discretization methods (*i.e.* boundary element method). Most of the related existing works deal with the second-order form of the time-harmonic Maxwell equations discretized by a conforming finite element method [30]. More recently, discontinuous Galerkin methods [24] have also been considered for this purpose. Here, we concentrate on the first-order form of the time-harmonic Maxwell equations discretized by discontinuous Galerkin methods on unstructured tetrahedral meshes.

Theoretical results concerning discontinuous Galerkin methods applied to the time-harmonic Maxwell equations have been obtained by several authors. Most of these works use a mixed formulation [31, 25] but discontinuous Galerkin methods on the non-mixed formulation have also been proved to converge (interior penalty techniques [24, 7] and local discontinuous Galerkin methods [7]). However, to our knowledge, a direct convergence analysis of discontinuous Galerkin methods applied to the first-order time-harmonic Maxwell system has not been conducted so far. Our contribution in [12] is a numerical study of the convergence of discontinuous Galerkin methods based on centered and upwind fluxes and nodal polynomial interpolation applied to the first-order time-harmonic Maxwell system in the two-dimensional case. These methods have previously been shown to converge in the time-domain case [23, 17].

In this paper, we are concerned with the application of such discontinuous Galerkin methods to the discretization of the three-dimensional time-harmonic Maxwell equations taken in the form of a first-order system of partial differential equations. Our efforts are towards the design of a parallel solution strategy for the resulting large, sparse and complex coefficients algebraic systems. Indeed, as far as non-trivial propagation problems are considered, the associated matrix operators are in most cases solved with difficulty by classical iterative methods. The preconditioning issues for highly indefinite and non-symmetric matrices is for instance discussed by Benzi *et al.* in [3] in the context of incomplete factorization and sparse approximate inverse preconditioners. If a robust and efficient solver is sought then a sparse direct method is the most practical choice. Over the last decade, significant progress has been made in developing parallel direct methods for solving sparse linear systems, due in particular to advances made in both the combinatorial analysis of Gaussian elimination process, and on the design of parallel block solvers optimized for high-performance computers [2, 22]. However, direct methods will still fail to solve very large three-dimensional problems, due to the potentially huge memory requirements for these cases. Iterative methods can be used to overcome this memory problem. However, a better solution can be found, combining advantages of both iterative and direct methods. For example, a popular approach is domain decomposition where one splits the computational domain into smaller subdomains and then

uses a direct solver inside each subdomain coupled with an iterative solver on the interfaces (artificial boundaries) between subdomains. This approach is adopted in this work.

Domain decomposition methods are flexible and powerful techniques for the parallel numerical solution of systems of partial differential equations. Concerning their application to time-harmonic wave propagation problems, the simplest algorithm was proposed by Després [10] for solving the Helmholtz equation and then extended and generalized for the time-harmonic Maxwell equations in [11, 9, 1]. The analysis of a larger class of Schwarz algorithms has been performed recently in [13]. Our ultimate objective is the design and application of optimized Schwarz algorithms in conjunction with discontinuous Galerkin methods. The first step in this direction is understanding and analyzing classical overlapping and non-overlapping Schwarz algorithms in the discrete framework of these methods. To our knowledge, except in Helluy [20], where such an algorithm is applied to a discretization of the first-order time-harmonic Maxwell equations by an upwind finite volume method, no other attempts for higher order discontinuous Galerkin methods or different kind of fluxes can be found in the literature. A classical domain decomposition strategy is adopted in this study which takes the form of a Schwarz-type algorithm where Després conditions [11] are imposed at the interfaces between neighboring subdomains. A multifrontal sparse direct solver is used at the subdomain level. The resulting domain decomposition strategy can be viewed as a hybrid iterative/direct solution method for the large, sparse and complex coefficients algebraic system resulting from the discretization of the time-harmonic Maxwell equations by a discontinuous Galerkin method.

The rest of this paper is organized as follows. In section 2, we formulate the continuous boundary value problem to be solved. Then, in section 3, the adopted Schwarz-type domain decomposition method is introduced. Section 4 is devoted to the discretization of the global and domain decomposed boundary value problems. A well-posedness result for a perturbed discrete problem which generalizes the idea of [6] to higher order discontinuous Galerkin methods is established. Finally, in section 5, numerical strategies for solving local problems as well as parallel computing aspects are discussed and experimental results are presented. Beside classical scattering test problems, we also consider a more challenging situation which consists in the propagation of a plane wave in a realistic geometric model of human head tissues.

2 Formulation of the continuous problem

The system of non-dimensioned time-harmonic Maxwell's equations can be written under the following form :

$$\begin{cases} \mathrm{i}\omega\varepsilon_r \boldsymbol{E} - \operatorname{curl} \boldsymbol{H} = -\boldsymbol{J}, \\ \mathrm{i}\omega\mu_r \boldsymbol{H} + \operatorname{curl} \boldsymbol{E} = 0, \end{cases} \tag{1}$$

where $\boldsymbol{E}$ and $\boldsymbol{H}$ are the unknown electric and magnetic fields and $\boldsymbol{J}$ is a known current source. The parameters ε_r and μ_r are respectively the complex-valued relative dielectric permittivity (integrating the electric conductivity) and the relative magnetic permeability ;

we consider here the case of linear isotropic media. The angular frequency of the problem is given by ω. Equation (1) is solved in a bounded domain Ω. On the boundary $\partial\Omega = \Gamma_a \cup \Gamma_m$, the following boundary conditions are imposed :

$$\begin{aligned} &\text{- a perfect electric conductor (PEC) condition on } \Gamma_m : \boldsymbol{n} \times \boldsymbol{E} = 0, \\ &\text{- a Silver-Müller (first-order absorbing boundary) condition} \\ &\quad \text{on } \Gamma_a : \boldsymbol{n} \times \boldsymbol{E} + \boldsymbol{n} \times (\boldsymbol{n} \times \boldsymbol{H}) = \boldsymbol{n} \times \boldsymbol{E}^{\text{inc}} + \boldsymbol{n} \times (\boldsymbol{n} \times \boldsymbol{H}^{\text{inc}}). \end{aligned} \tag{2}$$

The vectors $\boldsymbol{E}^{\text{inc}}$ and $\boldsymbol{H}^{\text{inc}}$ represent the components of an incident electromagnetic wave and $\boldsymbol{n}$ denotes the unitary outward normal. Equations (1) and (2) can be further rewritten, assuming $\boldsymbol{J}$ equals to 0, under the following form :

$$\begin{cases} \mathrm{i}\omega G_0 \boldsymbol{W} + G_x \partial_x \boldsymbol{W} + G_y \partial_y \boldsymbol{W} + G_z \partial_z \boldsymbol{W} = 0 \text{ in } \Omega, \\ (M_{\Gamma_m} - G_{\boldsymbol{n}})\boldsymbol{W} = 0 \text{ on } \Gamma_m, \\ (M_{\Gamma_a} - G_{\boldsymbol{n}})(\boldsymbol{W} - \boldsymbol{W}^{\text{inc}}) = 0 \text{ on } \Gamma_a. \end{cases} \tag{3}$$

where $\boldsymbol{W} = \begin{pmatrix} \boldsymbol{E} \\ \boldsymbol{H} \end{pmatrix}$ is the new unknown vector and $G_0 = \begin{pmatrix} \varepsilon_r \, \mathrm{I}_3 & 0_{3\times 3} \\ 0_{3\times 3} & \mu_r \, \mathrm{I}_3 \end{pmatrix}$. The terms I_3 and $0_{3\times 3}$ denote respectively the identity matrix and a null matrix, of dimensions 3×3. The real part of G_0 is symmetric positive definite and its imaginary part, which appears for instance in the case of conductive materials, is symmetric negative. Denoting by $(\boldsymbol{e}^x, \boldsymbol{e}^y, \boldsymbol{e}^z)$ the canonical basis of $\mathbb{R}^3$, the matrices G_l with $l \in \{x, y, z\}$ are given by :

$$G_l = \begin{pmatrix} 0_{3\times 3} & N_{\boldsymbol{e}^l} \\ N^t_{\boldsymbol{e}^l} & 0_{3\times 3} \end{pmatrix} \text{ where for a vector } \boldsymbol{v} = \begin{pmatrix} v_x \\ v_y \\ v_z \end{pmatrix}, \; N_{\boldsymbol{v}} = \begin{pmatrix} 0 & v_z & -v_y \\ -v_z & 0 & v_x \\ v_y & -v_x & 0 \end{pmatrix}.$$

In the following we denote by $G_{\boldsymbol{n}}$ the sum $G_x n_x + G_y n_y + G_z n_z$ and by $G^+_{\boldsymbol{n}}$ and $G^-_{\boldsymbol{n}}$ its positive and negative parts[1]. We also define $|G_{\boldsymbol{n}}| = G^+_{\boldsymbol{n}} - G^-_{\boldsymbol{n}}$. In order to take into account the boundary conditions, the matrices M_{Γ_m} and M_{Γ_a} are given by :

$$M_{\Gamma_m} = \begin{pmatrix} 0_{3\times 3} & N_{\boldsymbol{n}} \\ -N^t_{\boldsymbol{n}} & 0_{3\times 3} \end{pmatrix} \quad \text{and} \quad M_{\Gamma_a} = |G_{\boldsymbol{n}}|.$$

3 A classical domain decomposition method

We consider now the problem (3). In order to ease the presentation we decompose the domain Ω into two overlapping or non-overlapping subdomains Ω_1 and Ω_2 but the extension of the formulation of the method to any number of subdomains is straightforward. We define $\Gamma_{12} = \partial\Omega_1 \cap \Omega_2$ and $\Gamma_{21} = \partial\Omega_2 \cap \Omega_1$. In the following we denote by $\boldsymbol{n}_{ij}$ the outward normal

[1] If $T\Lambda T^{-1}$ is the eigenfactorization of $G_{\boldsymbol{n}}$ then $G^{\pm}_{\boldsymbol{n}} = T\Lambda^{\pm}T^{-1}$ where Λ^+ (resp. Λ^-) only gathers the positive (resp. negative) eigenvalues.

vector to the interface Γ_{ij} with i,j in $\{1,2\}$. We solve system (3) in both subdomains and we enforce on the subdomain interfaces the continuity of the incoming characteristic variables which provides a so-called *classical Schwarz algorithm* (see [13] for details). The classical Schwarz algorithm allows to compute the $(n+1)$-th iterate of the solution from the n-th iterate, starting from an arbitrary initial guess, by solving local problems and then exchanging information between artificial boundaries, called interfaces. This algorithm is given by :

$$\left\{\begin{array}{l} i\omega\,\boldsymbol{W}^{1,n+1} + \displaystyle\sum_{l\in\{x,y,z\}} G_l\partial_l \boldsymbol{W}^{1,n+1} = 0 \text{ in } \Omega_1, \\ G^-_{\boldsymbol{n}_{12}}\boldsymbol{W}^{1,n+1} = G^-_{\boldsymbol{n}_{12}}\boldsymbol{W}^{2,n} \text{ on } \Gamma_{12}, \\ + \text{ Boundary conditions on } \partial\Omega_1 \cap \partial\Omega, \end{array}\right. \tag{4}$$

$$\left\{\begin{array}{l} i\omega\,\boldsymbol{W}^{2,n+1} + \displaystyle\sum_{l\in\{x,y,z\}} G_l\partial_l \boldsymbol{W}^{2,n+1} = 0 \text{ in } \Omega_2, \\ G^-_{\boldsymbol{n}_{21}}\boldsymbol{W}^{2,n+1} = G^-_{\boldsymbol{n}_{21}}\boldsymbol{W}^{1,n} \text{ on } \Gamma_{21}, \\ + \text{ Boundary conditions on } \partial\Omega_2 \cap \partial\Omega, \end{array}\right.$$

where subscripts denote components, and superscripts denote the subdomain number and the iteration count.

This algorithm has been analyzed in [13] and its convergence rate has been computed in the case of an infinite domain $\Omega = \mathbb{R}^3$.

4 Discretization

The subproblems of the Schwarz algorithm (4) are discretized using a discontinuous Galerkin formulation. In this section, we first introduce this discretization method in the one-domain case. Then, we state a well-posedness result for a perturbed discrete problem. Finally, we establish the discretization of the interface condition of algorithm (4) with respect to the adopted discontinuous Galerkin formulation.

Let Ω_h denote a discretization of the domain Ω into a union of conforming tetrahedral elements $\overline{\Omega}_h = \displaystyle\bigcup_{K\in\mathcal{T}_h} K$. We look for the approximate solution $\boldsymbol{W}_h = \begin{pmatrix}\boldsymbol{E}_h \\ \boldsymbol{H}_h\end{pmatrix}$ of (3) in $V_h \times V_h$ where the functional space V_h is defined by :

$$V_h = \left\{\boldsymbol{U} \in [L^2(\Omega)]^3 \;/\; \forall K \in \mathcal{T}_h,\;\; \boldsymbol{U}_{|K} \in \mathbb{P}_p(K)\right\}. \tag{5}$$

where $\mathbb{P}_p(K)$ denotes a space of vectors with polynomial components of degree at most p over the element K.

4.1 Discretization of the mono-domain problem

Following the presentation of Ern and Guermond [15, 16], the discontinuous Galerkin discretization of system (3) yields the formulation of the discrete problem :

$$\left\{\begin{array}{l} \text{Find } \boldsymbol{W}_h \text{ in } V_h \times V_h \text{ such that :} \\ \displaystyle\int_{\Omega_h} (\mathrm{i}\omega G_0 \boldsymbol{W}_h)^t \overline{\boldsymbol{V}} dv + \sum_{K\in\mathcal{T}_h} \int_K \left(\sum_{l\in\{x,y,z\}} G_l \partial_l(\boldsymbol{W}_h) \right)^t \overline{\boldsymbol{V}} dv \\ \displaystyle + \sum_{F\in\Gamma^m\cup\Gamma^a} \int_F \left(\frac{1}{2}(M_{F,K} - I_{FK} G_{\boldsymbol{n}_F}) \boldsymbol{W}_h \right)^t \overline{\boldsymbol{V}} ds \\ \displaystyle - \sum_{F\in\Gamma^0} \int_F (G_{\boldsymbol{n}_F} [\![\boldsymbol{W}_h]\!])^t \{\overline{\boldsymbol{V}}\} ds + \sum_{F\in\Gamma^0} \int_F (S_F [\![\boldsymbol{W}_h]\!])^t [\![\overline{\boldsymbol{V}}]\!] ds \\ \displaystyle = \sum_{F\in\Gamma^a} \int_F \left(\frac{1}{2}(M_{F,K} - I_{FK} G_{\boldsymbol{n}_F}) \boldsymbol{W}^{\mathrm{inc}} \right)^t \overline{\boldsymbol{V}} ds, \quad \forall \boldsymbol{V} \in V_h \times V_h, \end{array}\right. \tag{6}$$

where Γ^0, Γ^a and Γ^m respectively denote the set of interior (triangular) faces, the set of faces on Γ_a and the set of faces on Γ_m. The unitary normal associated to the oriented face F is $\boldsymbol{n}_F$ and I_{FK} stands for the incidence matrix between oriented faces and elements whose entries are given by :

$$I_{FK} = \left\{\begin{array}{l} 0 \text{ if the face } F \text{ does not belong to element } K, \\ 1 \text{ if } F \in K \text{ and their orientations match,} \\ -1 \text{ if } F \in K \text{ and their orientations do not match.} \end{array}\right.$$

We also define respectively the jump and the average of a vector $\boldsymbol{V}$ of $V_h \times V_h$ on a face F shared by two elements K and $\tilde{K}$:

$$[\![\boldsymbol{V}]\!] = I_{FK} \boldsymbol{V}_{|K} + I_{F\tilde{K}} \boldsymbol{V}_{|\tilde{K}} \quad \text{and} \quad \{\boldsymbol{V}\} = \frac{1}{2}\left(\boldsymbol{V}_{|K} + \boldsymbol{V}_{|\tilde{K}} \right).$$

Finally, the matrix S_F, which is hermitian positive, allows to penalize the jump of a field or of some components of this field on the face F and the matrix $M_{F,K}$, to be defined later, insures the asymptotic consistency with the boundary conditions of the continuous problem.

Problem (6) is often interpreted in terms of local problems in each element K of $\mathcal{T}_h$ coupled by the introduction of an element boundary term called numerical flux (see also [15]).

In this study, we consider two classical numerical fluxes, which lead to distinct definitions for matrices S_F and $M_{F,K}$:

- **a centered flux** (see [17] for the time-domain equivalent). In this case $S_F = 0$ for all the faces F and, for the boundary faces, we use :

$$M_{F,K} = \begin{cases} I_{FK} \begin{pmatrix} 0_{3\times 3} & N_{\boldsymbol{n}_F} \\ -N^t_{\boldsymbol{n}_F} & 0_{3\times 3} \end{pmatrix} \text{ if } F \in \Gamma^m, \\ |G_{\boldsymbol{n}_F}| \text{ if } F \in \Gamma^a. \end{cases} \tag{7}$$

- **an upwind flux** (see [32, 15]). In this case :

$$S_F = \begin{pmatrix} \alpha^E_F N_{\boldsymbol{n}_F} N^t_{\boldsymbol{n}_F} & 0_{3\times 3} \\ 0_{3\times 3} & \alpha^H_F N^t_{\boldsymbol{n}_F} N_{\boldsymbol{n}_F} \end{pmatrix},$$
$$M_{F,K} = \begin{cases} \begin{pmatrix} \eta_F N_{\boldsymbol{n}_F} N^t_{\boldsymbol{n}_F} & I_{FK} N_{\boldsymbol{n}_F} \\ -I_{FK} N^t_{\boldsymbol{n}_F} & 0_{3\times 3} \end{pmatrix} \text{ if } \in \Gamma^m, \\ |G_{\boldsymbol{n}_F}| \text{ if } F \in \Gamma^a, \end{cases} \tag{8}$$

with α^E_F, α^H_F and η_F equals to $1/2$ for homogeneous media.

REMARK **1** *The formulation of the discontinuous Galerkin scheme above (in particular, the centered and upwind fluxes) actually applies to homegeneous materials. For describing the flux in the inhomogeneous case, let us define :*

$$Z^K = \frac{1}{Y^K} = \sqrt{\frac{\mu_r}{\varepsilon_r}}, \; Z^F = \frac{Z^K + Z^{\tilde{K}}}{2} \text{ and } Y^F = \frac{Y^K + Y^{\tilde{K}}}{2}, \tag{9}$$

where $F = \overline{K} \cap \overline{\tilde{K}}$. With these definitions, the discontinuous Galerkin scheme in the inhomogeneous case can be written formally as (6) *but by modifying S_F as :*

$$S_F = \frac{1}{2} \begin{pmatrix} \frac{1}{Z^F} N_{\boldsymbol{n}_F} N^t_{\boldsymbol{n}_F} & 0_{3\times 3} \\ 0_{3\times 3} & \frac{1}{Y^F} N^t_{\boldsymbol{n}_F} N_{\mathbf{n}_F} \end{pmatrix}, \tag{10}$$

and by using for the average, a weighted average $\{\cdot\}_F$ for each face F :

$$\{\mathbf{V}\}_F = \frac{1}{2} \left(\begin{pmatrix} \frac{Z^{\tilde{K}}}{Z^F} & 0_{3\times 3} \\ 0_{3\times 3} & \frac{Y^{\tilde{K}}}{Y^F} \end{pmatrix} \mathbf{V}_{|K} + \begin{pmatrix} \frac{Z^K}{Z^F} & 0_{3\times 3} \\ 0_{3\times 3} & \frac{Y^K}{Y^F} \end{pmatrix} \mathbf{V}_{|\tilde{K}} \right). \tag{11}$$

In order to simplify the presentation in the following sections, we only retain the formulation adapted to homogeneous materials.

4.2 Comments on the discretization

A few works have considered the discretization of the time-harmonic Maxwell equations by a discontinuous Galerkin formulation combined to the numerical fluxes (7) and (8). Concerning the convergence properties of such discontinuous Galerkin formulations, the state-of-art is the following :

- when the discontinuous Galerkin method is combined to the upwind flux (8), convergence results have been obtained by Helluy and Dayma in [21] for a perturbed problem, *i.e.* replacing $\mathrm{i}\omega$ by $\mathrm{i}\omega+\nu$ with ν a strictly positive parameter. Their result states that, if the solution is sufficiently regular and if a polynomial approximation of order p is used in each element K, the L^2-norm error of the electromagnetic fields behaves as $h^{p+1/2}$ where h is the mesh parameter.
- the discontinuous Galerkin method combined to the centered flux (7) has been studied by Fezoui *et al.* in [17] for the time-domain Maxwell equations. In this case, the L^2-norm error of the electromagnetic fields behaves as h^p. This result should extend to the time-harmonic case however no convergence proofs are available so far.

The convergence of the discontinuous Galerkin methods considered here is studied numerically in the context of the two-dimensional time-harmonic Maxwell equations discretized on triangular meshes in [12].

Beside, we can study the solvability of the discrete problem in the case of a perturbed problem (we replace $\mathrm{i}\omega$ by $\mathrm{i}\omega+\nu$ with $\nu>0$). We reacll here the proff already presented in [12]. In this setting and assuming homogeneous boundary conditions, the problem at hand can be simply written as :

$$\begin{cases} \text{Find } \boldsymbol{W}_h \text{ in } V_h \times V_h \text{ such that :} \\ a(\boldsymbol{W}_h, \boldsymbol{V}) + b(\boldsymbol{W}_h, \boldsymbol{V}) = 0, \ \forall \boldsymbol{V} \in V_h \times V_h, \end{cases} \tag{12}$$

with, $\forall \boldsymbol{U}, \boldsymbol{V} \in V_h \times V_h$:

$$\begin{aligned} a(\boldsymbol{U}, \boldsymbol{V}) = & \int_{\Omega_h} ((\mathrm{i}\omega+\nu) G_0 \boldsymbol{U})^t \, \overline{\boldsymbol{V}} dv + \sum_{F \in \Gamma^a} \int_F \left(\frac{1}{2} |G_{\boldsymbol{n}_F}| \boldsymbol{U} \right)^t \overline{\boldsymbol{V}} ds \\ & + \sum_{F \in \Gamma^m} \int_F \left(\frac{1}{2} M_{F,K} \boldsymbol{U} \right)^t \overline{\boldsymbol{V}} ds + \sum_{F \in \Gamma^0} \int_F (S_F [\![\boldsymbol{U}]\!])^t \, [\![\overline{\boldsymbol{V}}]\!]_F ds, \end{aligned} \tag{13}$$

and :

$$\begin{aligned} b(\boldsymbol{U}, \boldsymbol{V}) = & \sum_{K \in \mathcal{T}_h} \int_K \left(\sum_{l \in \{x,y,z\}} G_l \partial_l(\boldsymbol{U}) \right)^t \overline{\boldsymbol{V}} dv \\ & - \sum_{F \in \Gamma^a \cup \Gamma^m} \int_F \left(\frac{1}{2} I_{FK} G_{\boldsymbol{n}_F} \boldsymbol{U} \right)^t \overline{\boldsymbol{V}} ds \\ & - \sum_{F \in \Gamma^0} \int_F (G_{\boldsymbol{n}_F} [\![\boldsymbol{U}]\!])^t \, \{\overline{\boldsymbol{V}}\} ds. \end{aligned} \tag{14}$$

Then, we have the following result.

PROPOSITION **1** *The solution of problem* (12) *is equal to zero.*

Proof Let $\Re(G_0)$ and $\Im(G_0)$ respectively denote the real and imaginary parts of G_0. First, considering the fact that the matrices $|G_{\boldsymbol{n}_F}|$, S_F, $\Re(G_0)$ and $-\Im(G_0)$ are hermitian and denoting by $\mathcal{H}(M_{F,K})$ the hermitian part of $M_{F,K}$ for F in Γ^m, which is equal to $\begin{pmatrix} \eta_F N_{\boldsymbol{n}_F} N_{\boldsymbol{n}_F}^t & 0_{3\times 3} \\ 0_{3\times 3} & 0_{3\times 3} \end{pmatrix}$, one has :

$$\begin{aligned} \Re(a(\boldsymbol{W}_h, \boldsymbol{W}_h)) = & \int_{\Omega_h} ((\nu\Re(G_0) - \omega\Im(G_0))\boldsymbol{W}_h)^t \, \overline{\boldsymbol{W}_h} dv \\ & + \sum_{F\in\Gamma^0} \int_F (S_F[\![\boldsymbol{W}_h]\!])^t \, [\![\overline{\boldsymbol{W}_h}]\!]_F ds \\ & + \sum_{F\in\Gamma^a} \int_F \left(\frac{1}{2}|G_{\boldsymbol{n}_F}|\boldsymbol{W}_h\right)^t \overline{\boldsymbol{W}_h} ds \\ & + \sum_{F\in\Gamma^m} \int_F \left(\frac{1}{2}\mathcal{H}(M_{F,K})\boldsymbol{W}_h\right)^t \overline{\boldsymbol{W}_h} ds. \end{aligned} \tag{15}$$

Then, we rewrite using the corresponding Green identity an equivalent expression of the sesquilinear form b :

$$\begin{aligned} b(\boldsymbol{U}, \boldsymbol{V}) = & -\sum_{K\in\mathcal{T}_h} \left[\int_K \boldsymbol{U}^t \left(\sum_{l\in\{x,y,z\}} G_l \partial_l(\overline{\boldsymbol{V}}) \right) dv \right. \\ & \left. - \sum_{F\in\partial K} \int_F (I_{FK} G_{\boldsymbol{n}_F} \boldsymbol{U}_{|K})^t \overline{\boldsymbol{V}}_{|K} ds \right] \\ & - \sum_{F\in\Gamma^a\cup\Gamma^m} \int_F \left(\frac{1}{2} I_{FK} G_{\boldsymbol{n}_F} \boldsymbol{U}\right)^t \overline{\boldsymbol{V}} ds \\ & - \sum_{F\in\Gamma^0} \int_F (G_{\boldsymbol{n}_F}[\![\boldsymbol{U}]\!])^t \{\overline{\boldsymbol{V}}\} ds, \ \forall \boldsymbol{U}, \boldsymbol{V} \in V_h \times V_h. \end{aligned} \tag{16}$$

By noticing that on a face $F \in \Gamma^0$ separating two elements K and $\tilde{K}$:

$$\begin{aligned} (G_{\boldsymbol{n}_F}\{\boldsymbol{U}\})^t[\![\boldsymbol{V}]\!] + (G_{\boldsymbol{n}_F}[\![\boldsymbol{U}]\!])^t\{\boldsymbol{V}\} = & (I_{FK} G_{\boldsymbol{n}_F} \boldsymbol{U}_{|K})^t \boldsymbol{V}_{|K} \\ & + (I_{F\tilde{K}} G_{\boldsymbol{n}_F} \boldsymbol{U}_{|\tilde{K}})^t \boldsymbol{V}_{|\tilde{K}}, \end{aligned}$$

which is in part due to the fact that $G_{\boldsymbol{n}_F}$ is hermitian, one deduces :

$$\begin{aligned} b(\boldsymbol{U},\boldsymbol{V}) = & -\sum_{K\in\mathcal{T}_h}\int_K \boldsymbol{U}^t\left(\sum_{l\in\{x,y,z\}} G_l\partial_l(\overline{\boldsymbol{V}})\right)dv \\ & + \sum_{F\in\Gamma^a\cup\Gamma^m}\int_F\left(\frac{1}{2}I_{FK}G_{\boldsymbol{n}_F}\boldsymbol{U}\right)^t\overline{\boldsymbol{V}}ds \\ & + \sum_{F\in\Gamma^0}\int_F\left(G_{\boldsymbol{n}_F}\{\boldsymbol{U}\}\right)^t[\![\overline{\boldsymbol{V}}]\!]ds,\ \forall\boldsymbol{U},\boldsymbol{V}\in V_h\times V_h. \end{aligned} \tag{17}$$

Thus, it is now straightforward to see that b is anti-hermitian and consequently :

$$\begin{aligned} \Re(a(\boldsymbol{W}_h,\boldsymbol{W}_h)+b(\boldsymbol{W}_h,\boldsymbol{W}_h)) = & \int_{\Omega_h}((\nu\Re(G_0)-\omega\Im(G_0))\boldsymbol{W}_h)^t\overline{\boldsymbol{W}_h}dv \\ & + \sum_{F\in\Gamma^0}\int_F(S_F[\![\boldsymbol{W}_h]\!])^t[\![\overline{\boldsymbol{W}_h}]\!]_F ds \\ & + \sum_{F\in\Gamma^a}\int_F\left(\frac{1}{2}|G_{\boldsymbol{n}_F}|\boldsymbol{W}_h\right)^t\overline{\boldsymbol{W}_h}ds \\ & + \sum_{F\in\Gamma^m}\int_F\left(\frac{1}{2}\mathcal{H}(M_{F,K})\boldsymbol{W}_h\right)^t\overline{\boldsymbol{W}_h}ds, \end{aligned}$$

From (12), $\Re(a(\boldsymbol{W}_h,\boldsymbol{W}_h)+b(\boldsymbol{W}_h,\boldsymbol{W}_h))$ is also equal to zero. As $\nu\Re(G_0)-\omega\Im(G_0)$ is positive definite and $|G_{\boldsymbol{n}_F}|$, S_F and $\mathcal{H}(M_{F,K})$ are positive, the vector field $\boldsymbol{W}_h$ is zero. ■

4.3 Discretization of the domain decomposition algorithm

4.3.1 Discontinuous Galerkin formulation of the multi-domain problem

Let us now assume that the domain Ω is decomposed into N_s subdomains $\Omega=\bigcup_{i=1}^{N_s}\Omega_i$. A superscript i indicates that some notations are relative to the subdomain Ω_i and not to the whole domain Ω. Thus, we will refer to $\mathcal{T}_h^i$ and V_h^i with obvious definitions from those of $\mathcal{T}_h$ and V_h and we also define $\Gamma_m^i=\Gamma_m\cap\partial\Omega_i$, $\Gamma_a^i=\Gamma_a\cap\partial\Omega_i$ and $\Gamma_0^i=\Gamma_0\cap\partial\Omega_i$ with their corresponding sets of faces $\Gamma^{m,i}$, $\Gamma^{a,i}$ and $\Gamma^{0,i}$. Finally Γ^{ij} will denote the set of faces which belongs to $\Gamma_{ij}=\partial\Omega_i\cap\Omega_j$.

According to algorithm (4), the interface condition on Γ_{ij} writes as :

$$G^-_{\boldsymbol{n}_F}(\boldsymbol{W}_h^{i,n+1}-\boldsymbol{W}_h^{j,n})=0 \quad \text{for all } F \text{ belonging to } \Gamma^{ij},$$

where $\boldsymbol{W}_h^{i,n+1}$ denotes the approximation of $\boldsymbol{W}^{i,n+1}$ for $i=1,2$. Thus, the discontinuous Galerkin discretization of a local problem of algorithm (4) can be written using (6), as the

solution of the following problem :

$$
\left\{
\begin{array}{l}
\text{Find } \boldsymbol{W}_h^{i,n+1} \text{ in } V_h^i \times V_h^i \text{ such that :} \\
\displaystyle\int_{\Omega_h^i} \left(\mathrm{i}\omega G_0 \boldsymbol{W}_h^{i,n+1}\right)^t \overline{\boldsymbol{V}} dv + \sum_{K\in\mathcal{T}_h^i} \int_K \left(\sum_{l\in\{x,y,z\}} G_l \partial_l (\boldsymbol{W}_h^{i,n+1}) \right)^t \overline{\boldsymbol{V}} dv \\
+ \displaystyle\sum_{F\in\Gamma^{m,i}} \int_F \left(\frac{1}{2}(M_{F,K} - I_{FK} G_{\boldsymbol{n}_F}) \boldsymbol{W}_h^{i,n+1} \right)^t \overline{\boldsymbol{V}} ds \\
+ \displaystyle\sum_{F\in(\Gamma^{a,i}\cup\Gamma^{ij})} \int_F \left(I_{FK} G^-_{\boldsymbol{n}_F} \boldsymbol{W}_h^{i,n+1} \right)^t \overline{\boldsymbol{V}} ds \\
- \displaystyle\sum_{F\in\Gamma^{0,i}} \int_F \left(G_{\boldsymbol{n}_F} [\![\boldsymbol{W}_h^{i,n+1}]\!] \right)^t \{\overline{\boldsymbol{V}}\} ds \\
+ \displaystyle\sum_{F\in\Gamma^{0,i}} \int_F \left(S_F [\![\boldsymbol{W}_h^{i,n+1}]\!] \right)^t [\![\overline{\boldsymbol{V}}]\!] ds \\
= \displaystyle\sum_{F\in\Gamma^{a,i}} \int_F \left(I_{FK} G^-_{\boldsymbol{n}_F} \boldsymbol{W}^{\mathrm{inc}} \right)^t \overline{\boldsymbol{V}} ds \\
+ \displaystyle\sum_{F\in\Gamma^{ij}} \int_F \left(I_{FK} G^-_{\boldsymbol{n}_F} \boldsymbol{W}^{j,n} \right)^t \overline{\boldsymbol{V}} ds, \qquad \forall \boldsymbol{V} \in V_h^i \times V_h^i.
\end{array}
\right. \tag{18}
$$

4.3.2 Formulation of an interface system

In the two-domain case the Schwarz algorithm can be written formally as follows :

$$
\left\{
\begin{array}{l}
\mathcal{L}\boldsymbol{W}^{1,n+1} = \boldsymbol{f}^1, \text{ in } \Omega_1, \\
\mathcal{B}_1(\boldsymbol{W}^{1,n+1}) = \lambda^{1,n}, \text{ on } \Gamma_{12}, \\
+ \text{ Boundary conditions on } \partial\Omega_1 \cap \partial\Omega,
\end{array}
\right.
\qquad
\left\{
\begin{array}{l}
\mathcal{L}\boldsymbol{W}^{2,n+1} = \boldsymbol{f}^2, \text{ in } \Omega_2, \\
\mathcal{B}_2(\boldsymbol{W}^{2,n+1}) = \lambda^{2,n}, \text{ on } \Gamma_{21}, \\
+ \text{ Boundary conditions on } \partial\Omega_2 \cap \partial\Omega,
\end{array}
\right. \tag{19}
$$

and then :

$$
\left\{
\begin{array}{rcl}
\lambda^{1,n+1} & = & \mathcal{B}_1(\boldsymbol{W}^{2,n+1}) \text{ on } \Gamma_{12}, \\
\lambda^{2,n+1} & = & \mathcal{B}_2(\boldsymbol{W}^{1,n+1}) \text{ on } \Gamma_{21},
\end{array}
\right. \tag{20}
$$

where $\mathcal{L}$ is a linear differential operator, $\boldsymbol{f}^{1,2}$ denotes right hand sides associated to $\Omega_{1,2}$ and, $\mathcal{B}_1$ and $\mathcal{B}_2$ are the interface operators. The Schwarz algorithm (19)-(20) can be rewritten as :

$$
\left\{
\begin{array}{rcl}
\lambda^{1,n+1} & = & \mathcal{B}_1(\boldsymbol{W}^2(\lambda^{2,n}, \boldsymbol{f}^2)), \\
\lambda^{2,n+1} & = & \mathcal{B}_2(\boldsymbol{W}^1(\lambda^{1,n}, \boldsymbol{f}^1)),
\end{array}
\right.
$$

where $\boldsymbol{W}^j = \boldsymbol{W}^j(\lambda^j, \boldsymbol{f}^j)$ are the solution of the local problems. By linearity of the operators involved, an iteration of the Schwarz algorithm is equivalent to :

$$\boldsymbol{\lambda}^{n+1} = (\mathrm{Id} - \mathcal{T})\boldsymbol{\lambda}^n + \boldsymbol{d},$$

which is a fixed point iteration to solve the interface system :

$$\mathcal{T}\boldsymbol{\lambda} = \boldsymbol{g}, \tag{21}$$

where $\boldsymbol{\lambda} = (\boldsymbol{\lambda}^1, \boldsymbol{\lambda}^2)$. From the discrete point of view, the global problem on domain Ω can be written in the matrix form :

$$\begin{pmatrix} A_1 & 0 & R_1 & 0 \\ 0 & A_2 & 0 & R_2 \\ 0 & -B_2 & \mathrm{I} & 0 \\ -B_1 & 0 & 0 & \mathrm{I} \end{pmatrix} \begin{pmatrix} \boldsymbol{W}_h^1 \\ \boldsymbol{W}_h^2 \\ \boldsymbol{\lambda}_h^1 \\ \boldsymbol{\lambda}_h^2 \end{pmatrix} = \begin{pmatrix} \boldsymbol{f}_h^1 \\ \boldsymbol{f}_h^2 \\ \mathbf{0} \\ \mathbf{0} \end{pmatrix},$$

where $A_{1,2}$ are local matrices coupling only internal unknowns, $R_{1,2}$ express the coupling between internal unknowns and interface unknowns and the subscript h denotes the discrete counterpart of a given quantity (*e.g.* $\boldsymbol{\lambda}_h^{1,2}$ are the discretized unknown vectors corresponding to $\boldsymbol{\lambda}^{1,2}$). The elimination of the internal unknowns $\boldsymbol{W}_h^{1,2}$ leads to the discrete counterpart of the interface problem (21), $\mathcal{T}_h\boldsymbol{\lambda}_h = \boldsymbol{g}_h$, with :

$$\mathcal{T}_h = \begin{pmatrix} \mathrm{I} & B_2A_2^{-1}R_2 \\ \\ B_1A_1^{-1}R_1 & \mathrm{I} \end{pmatrix} \quad \text{and} \quad \boldsymbol{g}_h = \begin{pmatrix} B_2A_2^{-1}F^2 \\ \\ B_1A_1^{-1}F^1 \end{pmatrix},$$

where $\mathcal{T}_h$ and $\boldsymbol{g}_h$ are the discretization of $\mathcal{T}$ and $\boldsymbol{d}$. This system is further solved by a Krylov subspace method as discussed in the following section.

5 Numerical and performance results

5.1 Implemented formulations and experimental testbed

For this study, the implementation of the discontinuous Galerkin formulations described in section (4.1) has been limited to a $\mathbb{P}_0$ approximation with the centered flux (7) (which is equivalent to a finite volume method which will be referred as DG-$\mathbb{P}_0$-c in the sequel) and a $\mathbb{P}_1$ approximation (*i.e.* a linear discontinuous Galerkin method) with either the centered flux (7) or the upwind flux (8) and nodal polynomial basis functions (respectively referred as DG-$\mathbb{P}_1$-c and DG-$\mathbb{P}_1$-u in the sequel).

Unless otherwise indicated, computations have been performed in 64 bit arithmetic. The experimental testbed is a cluster of AMD Opteron 2 GHz dual nodes with 2 GB of RAM memory, interconnected by a Gigabit Ethernet switch. The computer codes for the DG-$\mathbb{P}_0$ and DG-$\mathbb{P}_1$ methods have been programmed in Fortran and the parallelization relies on the MPI (Message Passing Interface). The implementation of the domain decomposition solver requires a partitioning of the underlying tetrahedral mesh which is obtained using the MeTiS graph partitioning tool [26].

5.2 Solution strategies

An unpreconditioned BiCGstab(ℓ) Krylov subspace method [35] is used for the solution of the interface system (21). After different tests for assessing the convergence of the method and the associated computation time, the parameter ℓ has been set to 6. This method is adapted to linear systems involving non-symmetric matrices with complex spectrum. The convergence of the iterative solution of the interface system is evaluated in terms of the euclidian norm of the residual normalized to the norm of the right-hand side vector. The corresponding linear threshold has been set to $\varepsilon_i = 10^{-6}$. Each iteration of this Krylov subspace method requires a certain number of matrix-vector products with the interface matrix of system (21). Within the domain decomposition framework of algorithm (4), such a matrix-vector product translates into the solution of the subdomain discrete problems (18). For this purpose, several strategies have been considered :

- a preconditioned restarted GMRES(m) [34] (with $m = 10$) or a preconditioned BiCGstab(ℓ) (with $\ell = 1$) method where the preconditioner is taken to be a LU factorization computed and stored in single precision arithmetic using the MUMPS multifrontal sparse direct solver [2], while the Krylov subspace method works on double precision arithmetic vectors. In both cases, the linear threshold has been set to $\varepsilon_i = 10^{-6}$. These solution strategies will be referred respectively as `DD-gmres` and `DD-bicgl`.

- a LU factorization where the L and U factors are computed and stored in single precision (32 bits) arithmetic and an iterative refinement procedure is applied to recover double precision arithmetic (64 bits). More precisely, assuming that the linear system is $Ax = b$, the iterative refinement procedure is as follows :

  $x \leftarrow 0$
  REPEAT
  $r \leftarrow b - Ax$ % residual evaluation step.
  Solve $Ly = r$
  Solve $Uz = y$
  $x \leftarrow x + z$ % updating step.
  UNTIL $\| r \| < \varepsilon_l$

  where the triangular solves $Ly = r$ and $Uz = y$ are performed using single precision arithmetic while the residual evaluation and updating step are computed in double precision arithmetic. In practice, we set $\varepsilon_l = 10^{-10}$ and a maximum of five iterations of the above procedure. In the sequel, this solution strategy will be referred as `DD-itref`.

These strategies have been selected with the aim to reduce the memory requirements for storing the L and U factors and thus allowing to tackle large problems. We note that such mixed-precision strategies have recently been considered in the linear algebra community essentially for performance issues [27, 28] on modern high-performance processors. In these works, the mixing of single and double precision computations is performed in the context of an iterative refinement procedure. Here, the single precision L and U factors yield a very

accurate preconditioner and consequently, a few iterations of the preconditioned Krylov subspace methods are sufficient for solving the subdomain problems. In practice we use one iteration of BiCGstab and two iterations of GMRES.

In the following tables and figures :
- L_{min}, Lmax and L_{avg} respectively denote the minimum, maximum and average length of an edge in a given tetrahedral mesh,
- N_s is the number of subdomains which is also the number of processes involved in a parallel simulation,
- 'CPU' is the CPU time which is evaluated on each process of a parallel simulation and, for this reason, we give both the minimum and maximum values of this quantity,
- 'REAL' is the real (or elapsed) time of a parallel simulation,
- 'RAM' is the memory requirement for storing the L and U factors which is evaluated on each process of a parallel simulation and, as for the 'CPU' quantity, we give both the minimum and maximum values of this quantity.

5.3 Diffraction of a plane wave by a PEC sphere

The first test problem that we consider is the diffraction of a plane wave by a perfectly conducting sphere with radius $R = 1$ m centered at the origin. The artificial boundary on which the first-order absorbing condition (2) applies is defined by a sphere with radius $R_a = 1.5$ m centered at the origin. The medium is considered homogeneous with ε_r and μ_r equal to one. The frequency of the incident plane wave is F = 600 MHz and $\omega = 2\pi F/F_0$ with $F_0 = 300$ MHz. Its polarization is such that :

$$\boldsymbol{k} = (0, 0, -k_z)^t \quad , \quad \boldsymbol{E} = (E_x, 0, 0)^t \quad \text{and} \quad \boldsymbol{H} = (0, H_y, 0)^t.$$

Four tetrahedral meshes of increased resolution have been used and their characteristics are summarized in Table 1. Views of the triangulations in the plane Z=0.0 m are given on Figure 1. Note that the mesh with the finest resolution is such that $L_{avg}=\lambda/11$ while this ratio is equal to 6 for the mesh with the coarsest resolution. Numerical solutions are shown

Mesh	# vertices	# tetrahedra	L_{min} (m)	L_{max} (m)	L_{avg} (m)
M1	32,418	172,800	0.051990	0.152832	0.086657
M2	70,422	384,000	0.039267	0.118029	0.066279
M3	151,452	843,648	0.030206	0.091805	0.051038
M4	244,834	1,382,400	0.025665	0.078819	0.043431

TAB. 1 – Diffraction of a plane wave by a PEC sphere, F=600 MHz. Characteristics of the tetrahedral meshes ('#' refers to 'the number of').

on Figures 2 and 3 in the form of the contour lines in the plane Z=0.0 m of the E_x and E_y components. Figures 2(a) and 2(b) correspond to the analytical solution for this problem, expressed using Debye potentials [14]. Clearly, the solutions obtained on mesh M4 using the

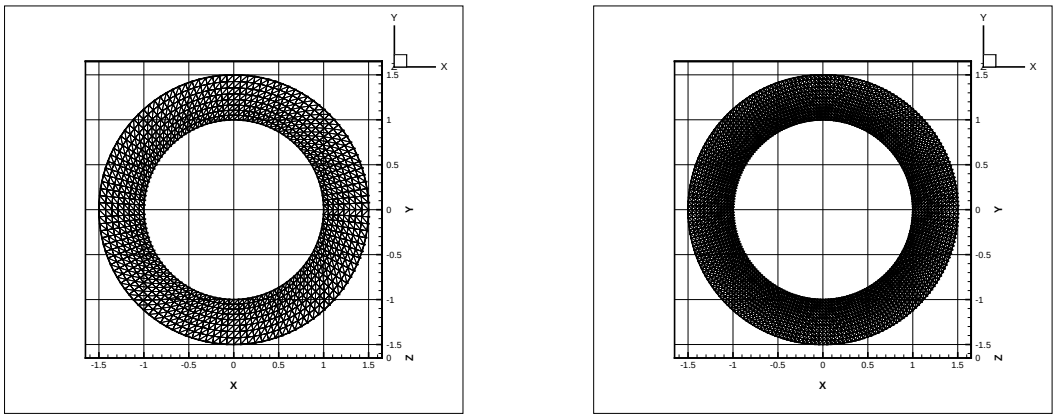

(a) mesh M1. (b) mesh M3.

FIG. 1 – Diffraction of a plane wave by a PEC sphere, F=600 MHz.
Triangulation in the plane Z=0.0 m.

DG-$\mathbb{P}_0$-c method, and on mesh M1 using the DG-$\mathbb{P}_1$-c/DG-$\mathbb{P}_1$-u methods are in very good agreement with the reference result.

Mesh	Method	Strategy	N_s	# it	CPU (min/max)	REAL
M1	DG-$\mathbb{P}_1$-c	DD-bicgl	32	10	441 sec/772 sec	929 sec
-	-	DD-gmres	-	10	227 sec/271 sec	442 sec
-	-	DD-itref	-	9	197 sec/300 sec	480 sec
M1	DG-$\mathbb{P}_1$-u	DD-bicgl	32	10	544 sec/616 sec	842 sec
-	-	DD-gmres	-	9	259 sec/284 sec	464 sec
-	-	DD-itref	-	9	170 sec/200 sec	344 sec
M2	DG-$\mathbb{P}_0$-c	DD-bicgl	16	8	215 sec/379 sec	390 sec
-	-	-	32	9	98 sec/132 sec	143 sec
-	-	DD-gmres	16	8	110 sec/139 sec	143 sec
-	-	-	32	9	46 sec/ 58 sec	68 sec
-	-	DD-itref	16	8	215 sec/379 sec	390 sec
-	-	-	32	9	101 sec/159 sec	172 sec
M3	DG-$\mathbb{P}_0$-c	DD-bicgl	32	8	244 sec/352 sec	456 sec
-	-	-	64	9	116 sec/178 sec	184 sec
-	-	DD-gmres	32	8	121 sec/164 sec	249 sec
-	-	-	64	9	56 sec/ 87 sec	98 sec
-	-	DD-itref	32	8	116 sec/197 sec	256 sec
-	-	-	64	9	53 sec/ 98 sec	111 sec
M4	DG-$\mathbb{P}_0$-c	DD-bicgl	64	9	197 sec/432 sec	460 sec
-	-	DD-gmres	-	10	109 sec/173 sec	211 sec
-	-	DD-itref	-	9	101 sec/193 sec	233 sec

TAB. 2 – Diffraction of a plane wave by a PEC sphere, F=600 MHz. Computation times (solution phase).

Mesh	Method	N_s	CPU (min/max)	RAM (min/max)
M1	DG-$\mathbb{P}_1$-c	32	198 sec/301 sec	1217 MB/1457 MB
M1	DG-$\mathbb{P}_1$-u	32	211 sec/329 sec	1257 MB/1512 MB
M2	DG-$\mathbb{P}_0$-c	8	220 sec/359 sec	1365 MB/1679 MB
-	-	16	56 sec/121 sec	492 MB/ 733 MB
-	-	32	11 sec/ 26 sec	156 MB/ 249 MB
M3	-	32	69 sec/185 sec	586 MB/ 959 MB
-	-	64	17 sec/ 52 sec	210 MB/ 370 MB
M4	-	64	43 sec/135 sec	425 MB/ 737 MB

TAB. 3 – Diffraction of a plane wave in vacuum by a PEC sphere, F=600 MHz. Computation times and memory requirement for storing the L and U factors.

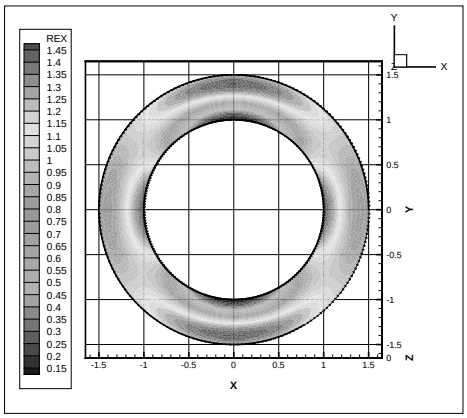

(a) Analytical solution, E_x.

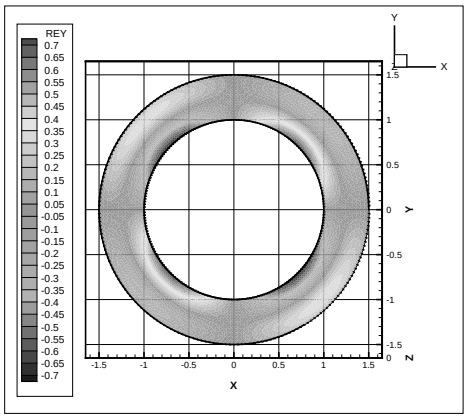

(b) Analytical solution, E_y.

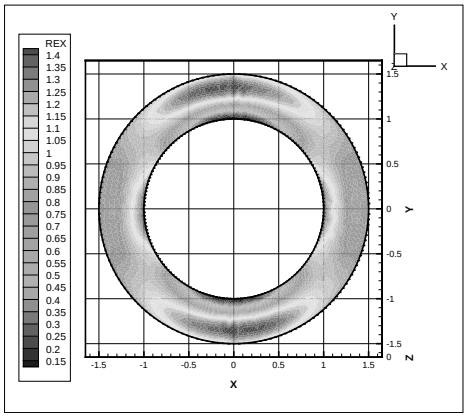

(c) Method DG-$\mathbb{P}_0$-c, mesh M2, E_x.

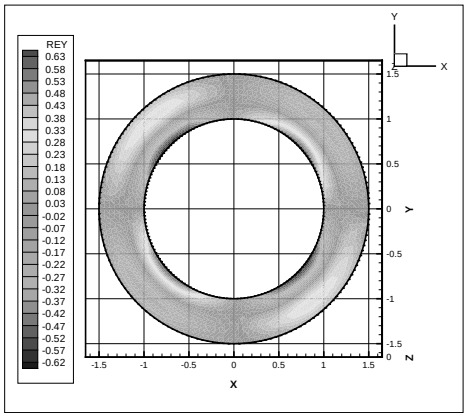

(d) Method DG-$\mathbb{P}_0$-c, mesh M2, E_y.

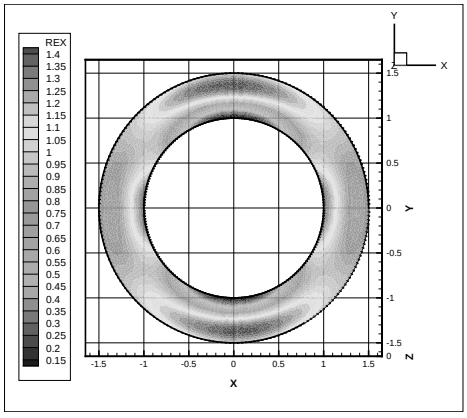

(e) Method DG-$\mathbb{P}_0$-c, mesh M3, E_x.

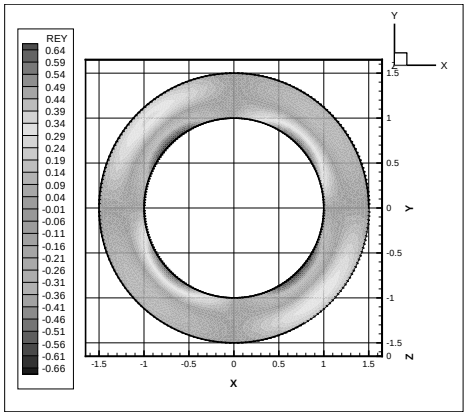

(f) Method DG-$\mathbb{P}_0$-c, mesh M3, E_y.

FIG. 2 – Diffraction of a plane wave by a PEC sphere, F=600 MHz.
Contour lines of E_x and E_y in the plane Z=0.0 m.

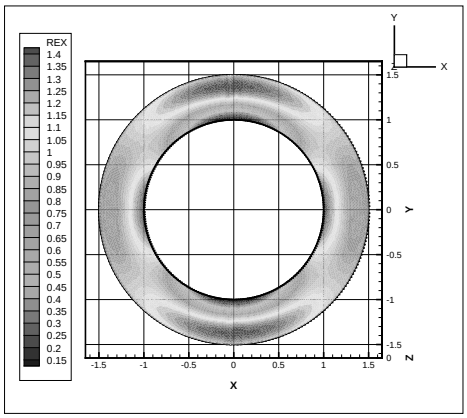

(a) Method DG-$\mathbb{P}_0$-c, mesh M4, E_x.

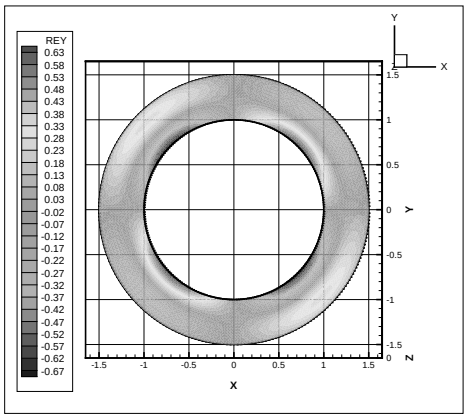

(b) Method DG-$\mathbb{P}_0$-c, mesh M4, E_y.

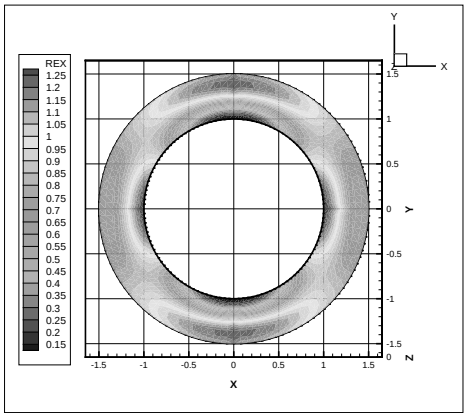

(c) Method DG-$\mathbb{P}_1$-c, mesh M1, E_x.

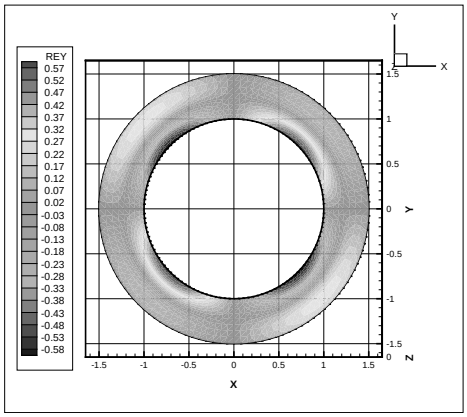

(d) Method DG-$\mathbb{P}_1$-c, mesh M1, E_y.

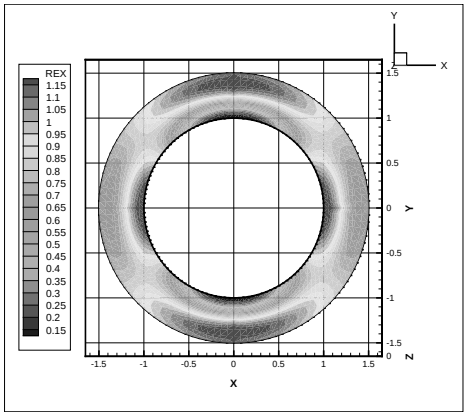

(e) Method DG-$\mathbb{P}_1$-u, mesh M1, E_x.

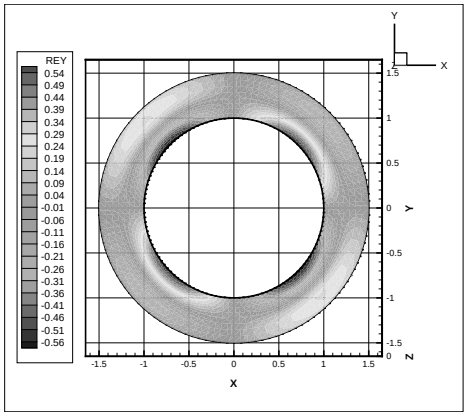

(f) Method DG-$\mathbb{P}_1$-u, mesh M1, E_y.

FIG. 3 – Diffraction of a plane wave by a PEC sphere, F=600 MHz.
Contour lines of E_x and E_y in the plane Z=0.0 m.

5.4 Diffraction of a plane wave by a PEC cube

The test problem considered here consists in the diffraction of a plane wave by a perfectly conducting cube of side length $C = 1/3$ m centered at the origin. The artificial boundary on which the first-order absorbing condition (2) applies is defined by a unitary cube centered at the origin. The frequency of the incident plane wave is F=900 MHz and its polarization is such that :

$$\boldsymbol{k} = (k_x, 0, 0)^t \quad , \quad \boldsymbol{E} = (0, E_y, 0)^t \quad \text{and} \quad \boldsymbol{H} = (0, 0, H_z)^t.$$

Five tetrahedral meshes have been used whose characteristics are summarized in Table 4 (see also Figure 4(a)). The exterior domain is always the vacuum but two situations have been considered for the cube : either it is strictly a perfect conductor or it is coated by a dielectric material with $\varepsilon_r = 4.0$ (see also Figure 4(b) for a view of the corresponding zone).

Mesh	# vertices	# tetrahedra	L_{min} (m)	L_{max} (m)	L_{avg} (m)
M1	9,136	46,704	0.05000	0.08660	0.06343
M2	29,062	156,000	0.03333	0.05773	0.04242
M3	67,590	373,632	0.02500	0.04330	0.03187
M4	129,276	725,424	0.02000	0.03464	0.02552
M5	220,122	1,248,000	0.01666	0.02886	0.02128

TAB. 4 – Diffraction of a plane wave by a PEC cube, F=900 MHz.
Characteristics of the tetrahedral meshes.

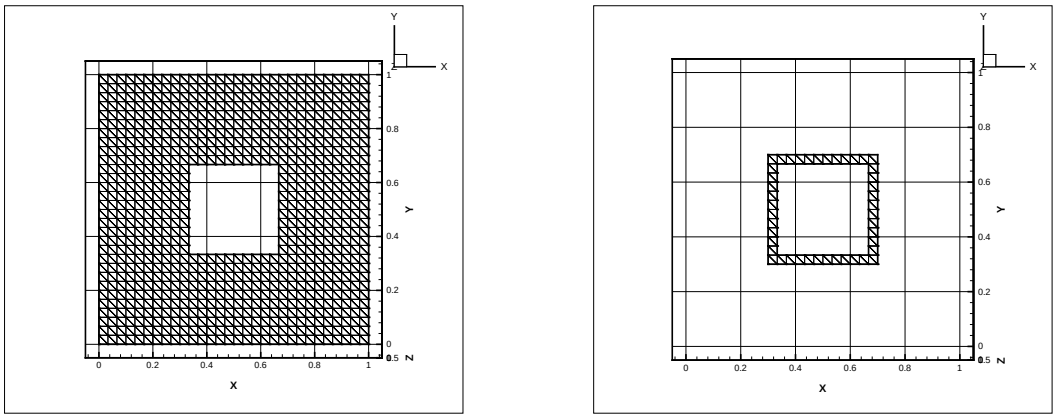

(a) Mesh example of the domain.

(b) Cube coated by a dielectric material.

FIG. 4 – Diffraction of a plane wave by a PEC cube, F=900 MHz.
Mesh M2 : triangulation in the plane Z=0.5 m.

5.4.1 Propagation in vacuum

Numerical solutions are shown on Figures 5 and 6 in the form of the contour lines in the plane Z=0.5 m of the E_x and E_y components. One can note that the solution resulting from the DG-$\mathbb{P}_1$-c method applied on mesh M1 is very similar to the one obtained using the DG-$\mathbb{P}_0$-c method with mesh M4. Moreover, the former solution exhibits a better symmetry with regards to the distribution of the E_y component. Timing measures are given in Table 5 (solution phase) and 6 (factorization phase).

Mesh	Method	Strategy	N_s	# it	CPU (min/max)	REAL
M1	DG-$\mathbb{P}_1$-c	DD-bicgl	8	6	202 sec/352 sec	355 sec
-	-	DD-gmres	-	6	106 sec/118 sec	124 sec
-	-	DD-itref	-	6	102 sec/130 sec	136 sec
M2	DG-$\mathbb{P}_1$-c	DD-bicgl	32	9	253 sec/440 sec	506 sec
-	-	-	64	10	105 sec/202 sec	236 sec
-	-	DD-gmres	32	9	115 sec/151 sec	207 sec
-	-	-	64	10	60 sec/ 82 sec	117 sec
-	-	DD-itref	32	9	108 sec/152 sec	168 sec
-	-	-	64	10	47 sec/ 72 sec	91 sec
M2	DG-$\mathbb{P}_1$-u	DD-bicgl	32	9	343 sec/389 sec	430 sec
-	-	-	64	10	161 sec/207 sec	234 sec
-	-	DD-gmres	32	9	170 sec/204 sec	258 sec
-	-	-	64	11	90 sec/116 sec	137 sec
-	-	DD-itref	32	9	114 sec/131 sec	174 sec
-	-	-	64	10	51 sec/ 69 sec	94 sec
M2	DG-$\mathbb{P}_0$-c	DD-bicgl	16	6	48 sec/ 61 sec	64 sec
-	-	DD-gmres	-	6	26 sec/ 32 sec	35 sec
-	-	DD-itref	-	6	20 sec/ 27 sec	31 sec
M3	DG-$\mathbb{P}_0$-c	DD-bicgl	16	7	150 sec/184 sec	199 sec
-	-	-	32	8	81 sec/101 sec	122 sec
M4	DG-$\mathbb{P}_0$-c	DD-bicgl	16	7	345 sec/395 sec	452 sec
-	-	-	32	8	161 sec/224 sec	238 sec
-	-	-	64	9	87 sec/108 sec	120 sec

TAB. 5 – Diffraction of a plane wave in vacuum by a PEC cube, F=900 MHz. Computation times (solution phase).

5.4.2 Coated PEC cube

Numerical solutions are shown on Figure 7 in the form of the contour lines in the plane Z=0.5 m of the E_x and E_y components. This time, we only report on results obtained using the DG-$\mathbb{P}_0$-c method applied to mesh M5 and the DG-$\mathbb{P}_1$-c/DG-$\mathbb{P}_1$-u methods applied to

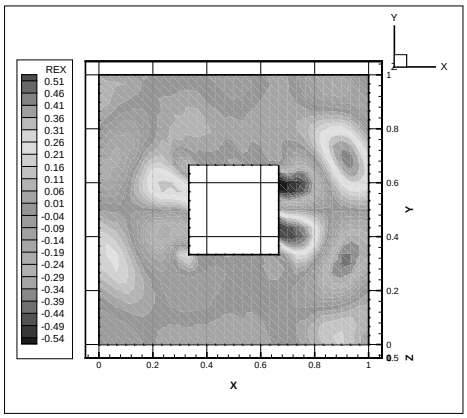

(a) Method DG-$\mathbb{P}_0$-c, mesh M2, E_x.

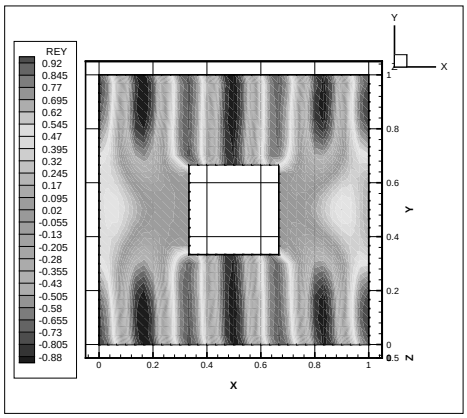

(b) Method DG-$\mathbb{P}_0$-c, mesh M2, E_y.

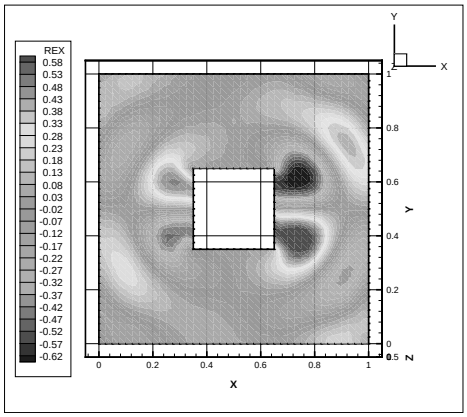

(c) Method DG-$\mathbb{P}_0$-c, mesh M3, E_x.

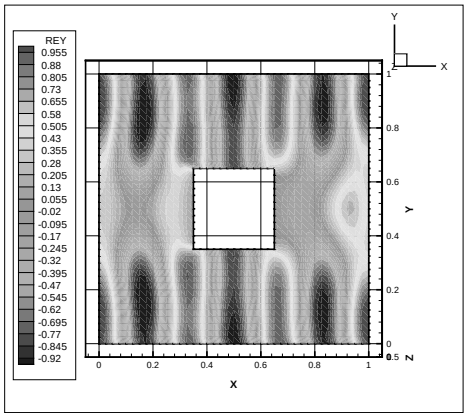

(d) Method DG-$\mathbb{P}_0$-c, mesh M3, E_y.

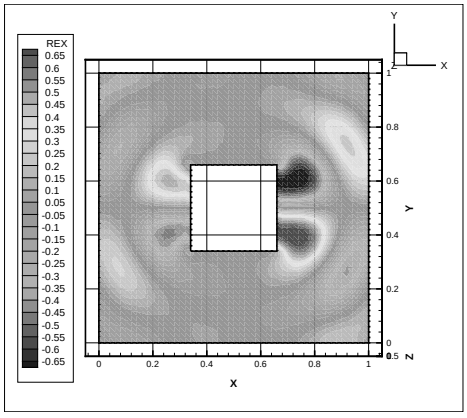

(e) Method DG-$\mathbb{P}_0$-c, mesh M4, E_x.

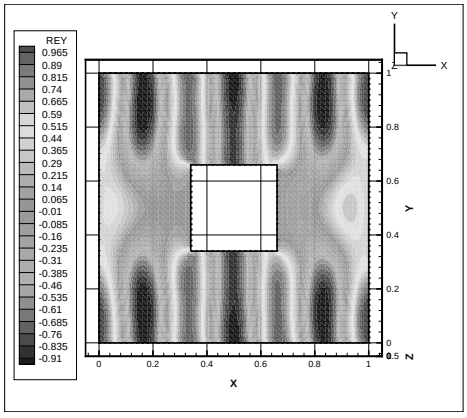

(f) Method DG-$\mathbb{P}_0$-c, mesh M4, E_y.

FIG. 5 – Diffraction of a plane wave in vacuum by a PEC cube, F=900 MHz. Contour lines of E_x and E_y in the plane Z=0.5 m.

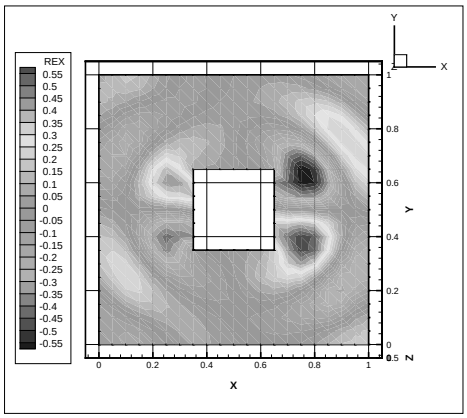

(a) Method DG-$\mathbb{P}_1$-c, mesh M1, E_x.

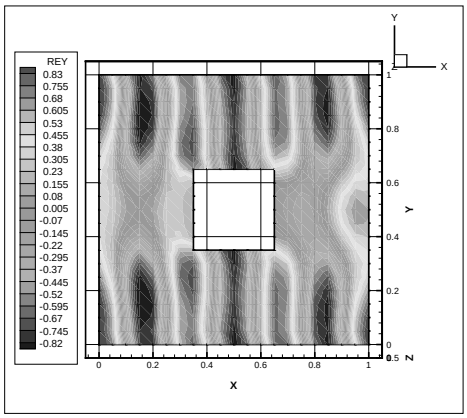

(b) Method DG-$\mathbb{P}_1$-c, mesh M1, E_y.

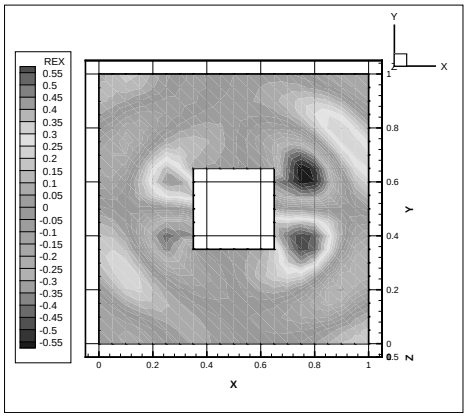

(c) Method DG-$\mathbb{P}_1$-c, mesh M2, E_x.

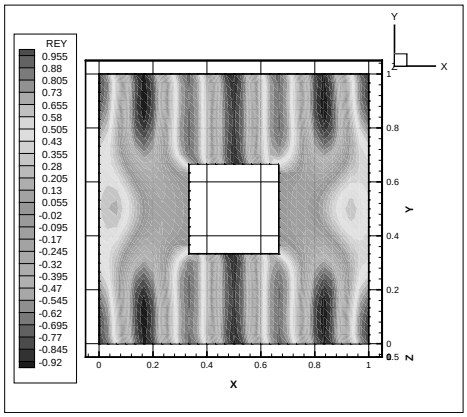

(d) Method DG-$\mathbb{P}_1$-c, mesh M2, E_y.

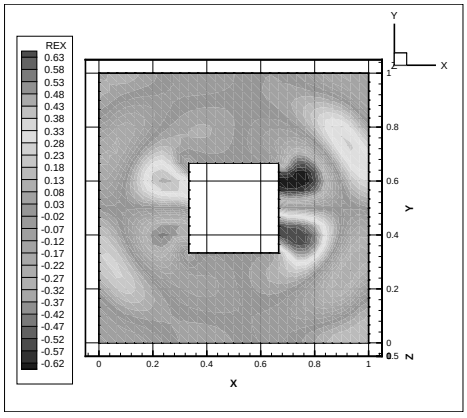

(e) Method DG-$\mathbb{P}_1$-u, mesh M2, E_x.

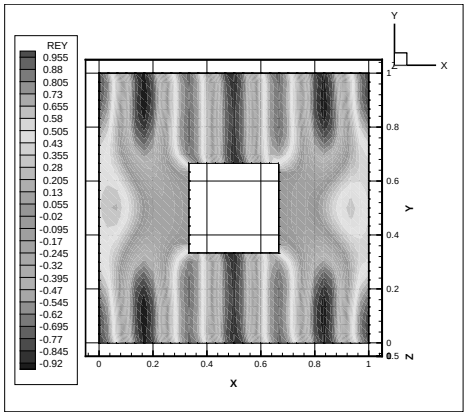

(f) Method DG-$\mathbb{P}_1$-u, mesh M2, E_y.

FIG. 6 – Diffraction of a plane wave in vacuum by a PEC cube, F=900 MHz.
Contour lines of E_x and E_y in the plane Z=0.5 m.

Mesh	Method	N_s	CPU (min/max)	RAM (min/max)
M1	DG-$\mathbb{P}_1$-c	8	82 sec/129 sec	735 MB/905 MB
M2	DG-$\mathbb{P}_1$-c	32	71 sec/105 sec	614 MB/728 MB
-	-	64	17 sec/ 32 sec	217 MB/295 MB
M2	DG-$\mathbb{P}_1$-u	32	88 sec/143 sec	710 MB/874 MB
-	-	64	20 sec/ 36 sec	243 MB/329 MB
M2	DG-$\mathbb{P}_0$-c	16	5 sec/ 8 sec	82 MB/105 MB
M3	-	16	23 sec/ 36 sec	285 MB/359 MB
-	-	32	7 sec/ 10 sec	104 MB/134 MB
M4	-	16	76 sec/114 sec	732 MB/884 MB
-	-	32	21 sec/ 37 sec	265 MB/359 MB
-	-	64	6 sec/ 10 sec	96 MB/129 MB

TAB. 6 – Diffraction of a plane wave in vacuum by a PEC cube, F=900 MHz. Computation times and memory requirement for storing the L and U factors.

mesh M2. One can note that the solution resulting from the DG-$\mathbb{P}_0$-c method does not exhibit all the peculiarities of the underlying wave propagation problem. This is made particularly clear on the distributions of the E_x component which suggest that the DG-$\mathbb{P}_0$-c might require a discretization mesh with an increased resolution. Timing measures are given in Tables 7 (solution phase) and 8 (factorization phase).

Mesh	Method	Strategy	N_s	# it	CPU (min/max)	REAL
M2	DG-$\mathbb{P}_1$-c	`DD-bicgl`	32	14	375 sec/643 sec	678 sec
-	-	`DD-gmres`	-	14	198 sec/236 sec	256 sec
-	-	`DD-itref`	-	14	173 sec/247 sec	271 sec
M2	DG-$\mathbb{P}_1$-u	`DD-bicgl`	32	13	471 sec/562 sec	630 sec
-	-	`DD-gmres`	-	13	245 sec/290 sec	317 sec
-	-	`DD-itref`	-	13	156 sec/184 sec	215 sec
M5	DG-$\mathbb{P}_0$-c	`DD-bicgl`	64	14	247 sec/310 sec	339 sec
-	-	`DD-gmres`	-	14	130 sec/164 sec	185 sec
-	-	`DD-itref`	-	14	98 sec/133 sec	157 sec

TAB. 7 – Diffraction of a plane wave by a coated PEC cube, F=900 MHz. Computation times (solution phase).

5.5 Discussion of the numerical and parallel performances

A first noticeable behaviour that can be emphasized is that the convergence of the proposed domain decomposition solver for a given approximation method is weakly dependent on the number of system unknowns and the granularity of the decomposition (*i.e.* the num-

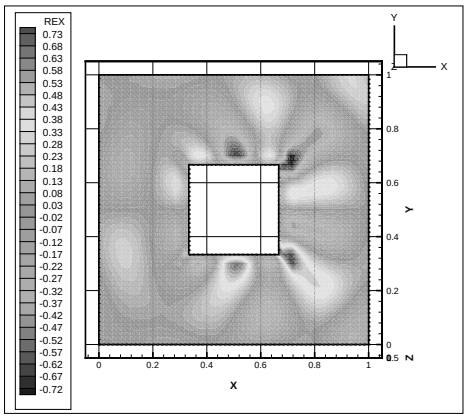

(a) Method DG-$\mathbb{P}_0$-c, mesh M5, E_x.

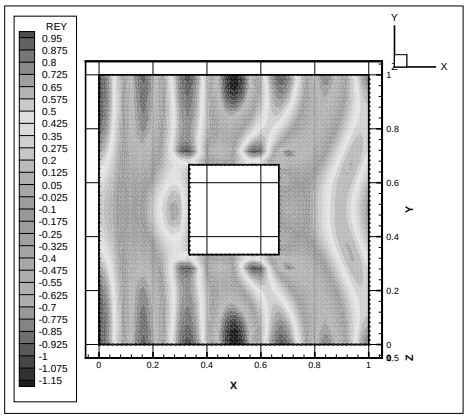

(b) Method DG-$\mathbb{P}_0$-c, mesh M5, E_y.

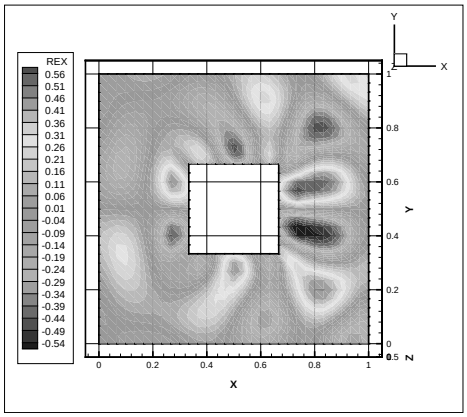

(c) Method DG-$\mathbb{P}_1$-c, mesh M2, E_x.

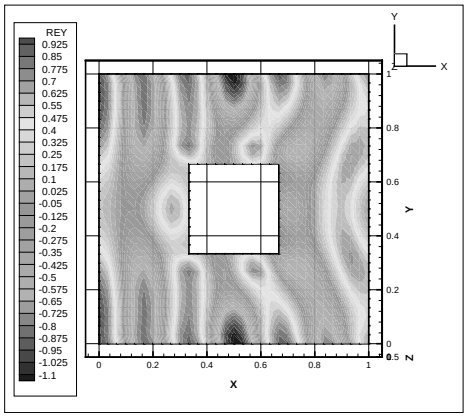

(d) Method DG-$\mathbb{P}_1$-c, mesh M2, E_y.

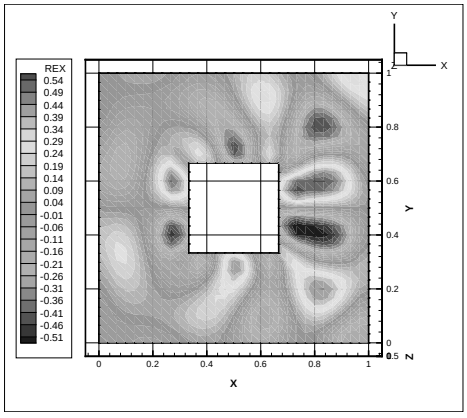

(e) Method DG-$\mathbb{P}_1$-u, mesh M2, E_x.

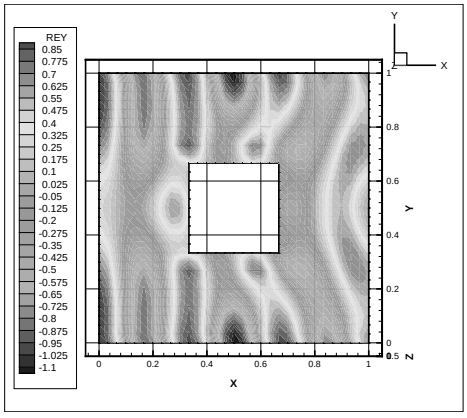

(f) Method DG-$\mathbb{P}_1$-u, mesh M2, E_y.

FIG. 7 – Diffraction of a plane wave by a coated PEC cube, F=900 MHz.
Contour lines of E_x and E_y in the plane Z=0.5 m.

Mesh	Method	N_s	CPU (min/max)	RAM (min/max)
M2	DG-$\mathbb{P}_1$-c	32	71 sec/102 sec	614 MB/728 MB
M2	DG-$\mathbb{P}_1$-u	32	87 sec/143 sec	710 MB/874 MB
M5	DG-$\mathbb{P}_0$-c	64	16 sec/ 29 sec	213 MB/299 MB

TAB. 8 – Diffraction of a plane wave by a coated PEC cube, F=900 MHz. Computation times and memory requirement for storing the L and U factors.

ber of subdomains). For instance, in the case of the diffraction of a plane wave by a PEC sphere, when switching from mesh M2 to mesh M4 (see Table 1), the number of unknowns of the algebraic system associated to the DG-$\mathbb{P}_0$-c approximation method increases from $6 \times 384,000 = 2,304,000$ to $6 \times 1,382,400 = 8,294,400$ while the number of iterations of the domain decomposition solver ranges from 8 to 10 for a number of subdomains N_s in the set $\{16, 32, 64\}$. Similarly, for the diffraction of a plane wave by a PEC cube, when switching from mesh M2 to mesh M4 (see Table 4), the number of unknowns of the algebraic system associated to the DG-$\mathbb{P}_0$-c approximation method increases from $6 \times 156,000 = 936,000$ to $6 \times 725,424 = 4,352,544$ while the number of iterations of the domain decomposition solver ranges from 6 to 9 for a number of subdomains N_s in the set $\{16, 32, 64\}$.

Moreover, for a given mesh, the number of iterations increases when switching between the DG-$\mathbb{P}_0$ and DG-$\mathbb{P}_1$ approximation methods. This is mainly related to the fact that at the same time the number of system unknowns increases noticeably. For instance, when simulating the diffraction of a plane wave by a PEC cube using mesh M2 (see Table 4), the number of system unknowns is equal to $6 \times 156,000 = 936,000$ and $24 \times 156,000 = 3,744,000$ respectively for the DG-$\mathbb{P}_0$ and DG-$\mathbb{P}_1$ approximation methods. In the former case, the number of iterations is equal to 6 for $N_s = 16$ while in the latter case, it is equal to 9 (respectively 10) for $N_s = 32$ (respectively 64).

It is also worthwhile to note that :

- the convergence of the domain decomposition solver when combined to the DG-$\mathbb{P}_1$ approximation method seems insensitive to the type of scheme (*i.e.* centered or upwind) used for the evaluation of the numerical flux through internal faces.
- as expected, when the propagation media is more complex than a simple uniform (*i.e.* homogeneous) material, the convergence of the domain decomposition solver requires more iterations. Indeed, comparing the performances of the domain decomposition solver combined to the DG-$\mathbb{P}_1$ approximation method for the simply PEC and coated PEC cubes and using mesh M2, the number of iterations increases from 9 to 14. Note that for mesh M5 and the DG-$\mathbb{P}_0$-c approximation method, the number of system unknowns is equal to $6 \times 1,248,000 = 7,488,000$ which is exactly twice the number obtained for the DG-$\mathbb{P}_1$ approximation method using mesh M2. Despite this large increase of the number of system unknowns and the difference in the number of subdomains (respectively $N_s = 32$ and $N_s = 64$), the solution of the underlying algebraic systems requires essentially the same number of iterations.

We evaluate the parallel performances of the proposed domain decomposition solver using two metrics : the ratio of the maximum of the per process CPU times to the REAL time which is referred as '%CPU' in the sequel and, the relative parallel speedup $S_{N_{s1}}^{N_{s2}}$ evaluated as the ratio of the elapsed time for N_{s1} subdomains to the elapsed time for N_{s2} subdomains. We mainly discuss the performance results of Table 2 but similar conclusions can be drawn based on the solution times given in Tables 5 and 7. First, we remark that, in the case of the diffraction of a plane wave by a PEC sphere, %CPU ranges from 58% to 97%. The lowest values of this metric are essentially obtained for the computations conducted with mesh M1 (see Table 1) which is due to the fact that the underlying mesh is too coarse and the communication cost induced by the BiCGstab(ℓ) method, which is applied to the solution of the interface system (21), prevails. Apart from this particular situation, one can note that super-linear parallel speedups are often obtained, For instance, for the same test case and computations based on mesh M2 (respectively M3), the $S_{16}^{32} \in [2.1\ ,\ 2.7]$ (respectively $S_{32}^{64} \in [2.3\ ,\ 2.5]$). This behaviour essentially stems from the super-linear reduction of the cost of the local solves when increasing the number or subdomains for a constant global problem size.

On the other hand, it is equally important to observe that although the MeTiS partitioning tool almost always yields well balanced partitions (in the present case, the load balance is evaluated in terms of the local number of tetrahedra), there is a noticeable disparity in the required amount of RAM for storing the subdomain L and U factors, especially for large values of the number of subdomains N_s. As a matter of fact, the fill-in of the L and U factors is influenced by several factors among which, the presence in the original matrix of diagonal blocks related to physical boundaries (metallic wall, absorbing boundary) which in turn has effects on the numerical pivoting strategy. But, above all, the partitioning of a mesh (in practice, the adjacency graph associated to the mesh) using a tool such as MeTiS, is dictated by two main criteria, namely the minimization of the subdomains separator and the achievement of a well balanced computational load, while a balance of the fill-in is rarely an objective. In the present case, the main consequence of this load unbalance in the fill-in of the local L and U factors is a potentially large gap between the minimum and maximum CPU times for the subdomain triangular solves, which results in non-negligible idle times across processes between each iteration of the interface system solver.

5.6 A bioelectromagnetics application

We conclude this section of results with the application of the proposed numerical methodology to the simulation of a time-harmonic electromagnetic wave propagation problem in an irregularly shaped and heterogeneous medium. The problem under consideration is concerned with the propagation of a plane wave in realistic geometrical models of head tissues. It is a first step towards the development of a computational framework for the numerical dosimetry of electromagnetic fields radiated by mobile phones. Starting from MR images of the Visible Human 2.0 project [33], head tissues are segmented and the interfaces of a selected number of tissues (namely, the skin, the skull and the brain) are triangulated.

Different strategies can be used in order to obtain a smooth and accurate segmentation of head tissues and interface triangulations as well. A first strategy consists in using a marching cube algorithm [29] which leads to huge triangulations of interfaces between segmented subdomains. These triangulations can then be regularized, refined and decimated in order to obtain reasonable surface meshes, for example using the YAMS [18] re-meshing tool. Another strategy consists in using a variant of Chew's algorithm [8], based on Delaunay triangulation restricted to the interface, which allows to control the size and aspect ratio of interfacial triangles [5]. Surface meshes of increased resolution resulting from such a procedure are presented on Figure 8. Then, these triangulated surfaces together with a triangulation of the artificial boundary (absorbing boundary) of the overall computational domain, which is taken here to be a sphere, are used as inputs for the generation of volume meshes. In this study, the GHS3D tetrahedral mesh generator [19] is used to mesh volume domains between the various interfaces. Two tetrahedral meshes have been used whose characteristics are summarized in Table 9. The frequency of the incident plane wave is F=1800 MHz and its polarization is such that :

$$\boldsymbol{k} = (k_x, 0, 0)^t \quad , \quad \boldsymbol{E} = (0, 0, E_z)^t \quad \text{and} \quad \boldsymbol{H} = (0, H_y, 0)^t.$$

Albeit this propagation problem clearly involves irregularly shaped domains and non-uniform tetrahedral meshes, it is yet a simplified configuration with regards to the simulations usually used in numerical dosimetry studies of human exposition to mobile phone radiation [4], for two reasons : a mobile phone geometrical model has not been taken into account in the present simulation setting and, the electromagnetic parameters of the materials are set to artificial values for the purpose of exemplifying the characteristics of the propagation of the plane wave in the head tissues (null conductivity, $\varepsilon_r = 4.0$ for the brain, $\varepsilon_r = 6.5$ for the cerebrospinal fluid, $\varepsilon_r = 1.5$ for the skull and $\varepsilon_r = 4.0$ for the skin). For the computations reported here, the methods DG-$\mathbb{P}_1$-c and DG-$\mathbb{P}_1$-u are used in conjunction with mesh M1 while method DG-$\mathbb{P}_0$-c is used with mesh M2. Moreover, this problem has also been simulated using a DGTD-$\mathbb{P}_1$-c (Discontinuous Galerkin Time-Domain) method [17] and the corresponding result will be considered here as the reference solution. The contour lines of E_z in various configurations are visualized on Figures 10 to 13. As can be seen on these figures, on one hand, there is a good agreement between the results of the time-domain and time-harmonic computations and, on the other hand, the DG-$\mathbb{P}_1$ methods used with the coarsest mesh yield solutions which are closer to the reference computation than the one resulting from the DG-$\mathbb{P}_0$-c method applied on the finest geometrical model.

Performance results are given in Tables 10 and 11. In addition, the convergence curves for the iterative solution of the interface system (21) using the BiCGstab(ℓ) method are shown on Figure 9. Firstly, we note that the iterative solution requires 3 to 4 times more iterations than the numbers observed for the previous test cases, which is the consequence of the increased complexity in both the underlying discretization and the propagation medium. Secondly, the parallel efficiency, evaluated using the %CPU ratio, ranges from 65% to 75%. Here again, the load unbalance in the fill-in of the local L and U factors is the main reason for this parallel performance drop.

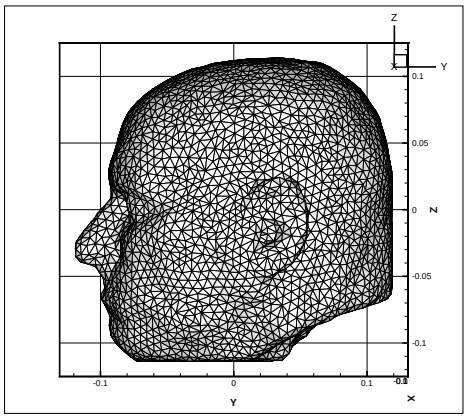

(a) Skin, lateral view, mesh M1.

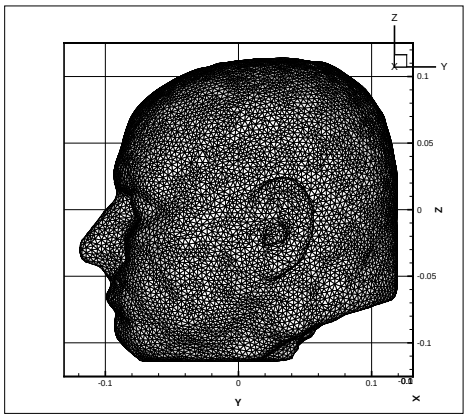

(b) Skin, lateral view, mesh M2.

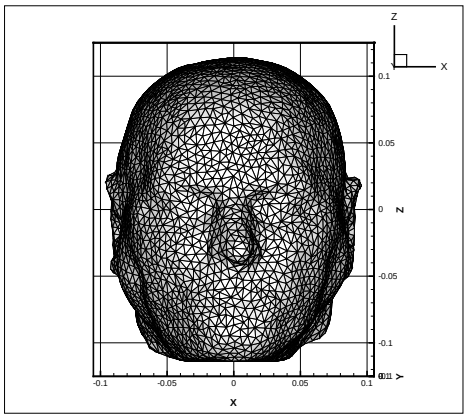

(c) Skin, frontal view, mesh M1.

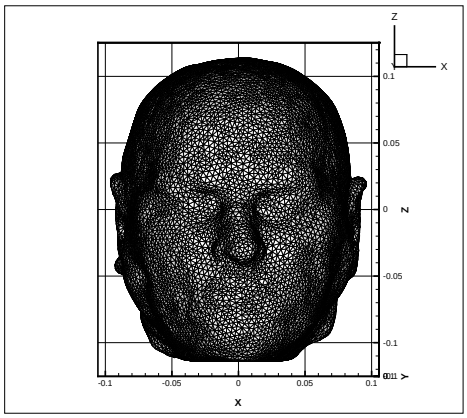

(d) Skin, lateral view, mesh M2.

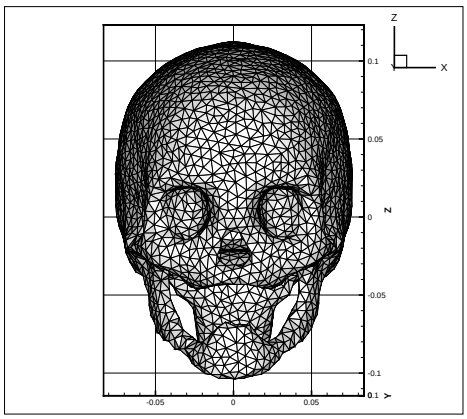

(e) Skull, frontal view, mesh M1.

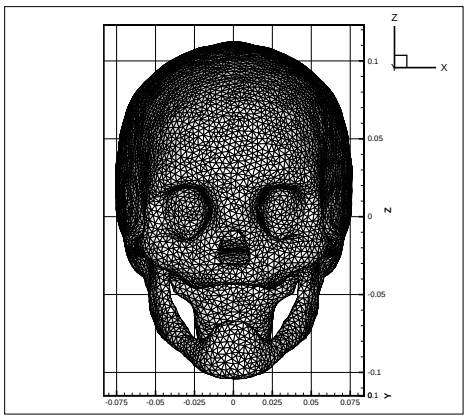

(f) Skull, frontal view, mesh M2.

FIG. 8 – Propagation of a plane wave in a heterogeneous medium, F=1800 MHz. Triangulations of the skin and the skull.

Mesh	# vertices	# tetrahedra	L_{min} (m)	L_{max} (m)	L_{avg} (m)
M1	60,590	361,848	0.00185	0.04537	0.01165
M2	309,599	1,853,832	0.00158	0.02476	0.00693

TAB. 9 – Propagation of a plane wave in a heterogeneous medium, F=1800 MHz. Characteristics of the tetrahedral meshes.

Mesh	Method	Strategy	N_s	# it	CPU (min/max)	REAL
M1	DG-$\mathbb{P}_1$-c	`DD-itref`	96	47	346 sec/466 sec	714 sec
-	DG-$\mathbb{P}_1$-u	`DD-itref`	96	46	347 sec/547 sec	765 sec
M2	DG-$\mathbb{P}_0$-c	`DD-itref`	96	33	228 sec/322 sec	428 sec

TAB. 10 – Propagation of a plane wave in an heterogeneous medium, F=1800 MHz. Computation times (solution phase).

Mesh	Method	N_s	CPU (min/max)	RAM (min/max)	# dof
M1	DG-$\mathbb{P}_1$-c	96	64 sec/125 sec	640 MB/852 MB	8,684,352
-	DG-$\mathbb{P}_1$-u	96	80 sec/134 sec	633 MB/866 MB	8,684,352
M2	DG-$\mathbb{P}_0$-c	96	53 sec/ 98 sec	519 MB/684 MB	11,122,992

TAB. 11 – Propagation of a plane wave in a heterogeneous medium, F=1800 MHz. Computation times and memory requirement for storing the L and U factors.

5.7 Conclusion

We have presented a hybrid iterative/direct solution method for the large, sparse and complex coefficients algebraic systems resulting from the discretization of the time-harmonic Maxwell equations by discontinuous Galerkin methods. The discretization in space relies on an unstructured tetrahedral mesh and as a result, the proposed numerical methodology is particularly well suited to the simulation of wave propagation problems in irregularly shaped media. Moreover, the local nature of a discontinuous Galerkin formulation allows for a natural treatment of heterogeneous media. Numerical and performance results reported here, albeit promising, have also raised a weakness in the current implementation of the domain decomposition method in the fact that the fill-in of the local L and U factors is generally not well balanced except for relatively simple problems (simply shaped domain, uniform mesh and homogeneous media). We believe that this drawback should be recurrent to almost all similar implementations of domain decomposition algorithms (*i.e.* based on exact factorization methods for the subdomain solves). This problem could be figure out by resorting to constrained level of fill-in subdomain solvers or/and by improving the quality of the mesh partitions (with regards to the resulting fill-in unbalance). In addition to these directions, our future works will be towards the improvement of the numerical efficiency of

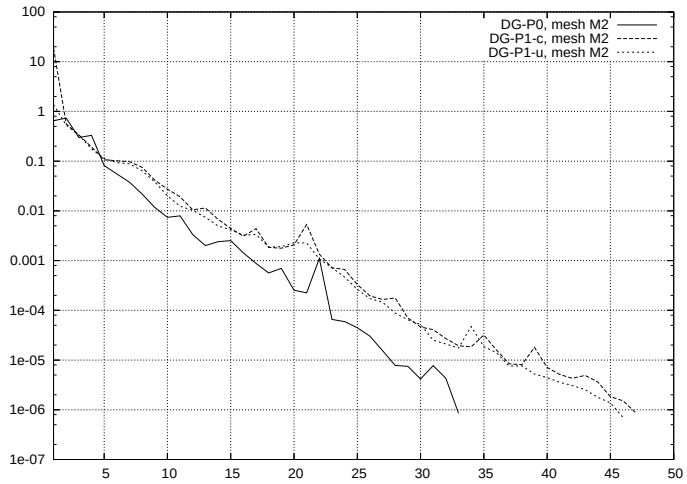

FIG. 9 – Propagation of a plane wave in a heterogeneous medium, F=1800 MHz. Iterative solution of the interface system.

the Schwarz-type algorithm adopted in this study thanks to the design of discrete optimized interface conditions [13] in the framework of our discontinuous Galerkin formulations on tetrahedral meshes.

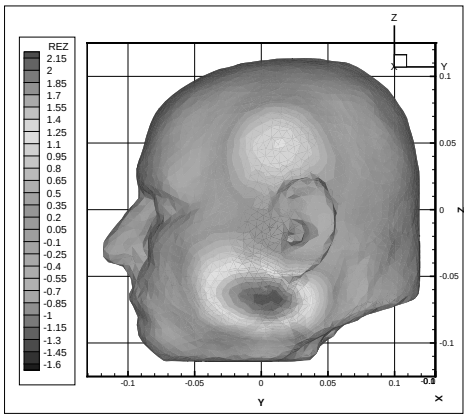

(a) method DG-$\mathbb{P}_1$-c, time-domain, skin, lateral view, mesh M1.

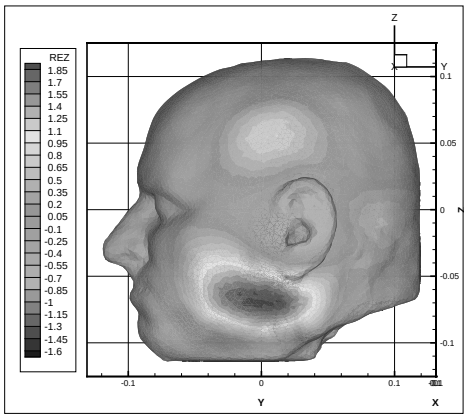

(b) method DG-$\mathbb{P}_0$-c, time-harmonic, skin, lateral view, mesh M2.

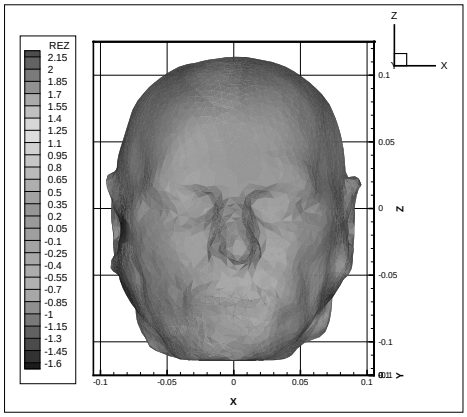

(c) method DG-$\mathbb{P}_1$-c, time-domain, skin, frontal view, mesh M1.

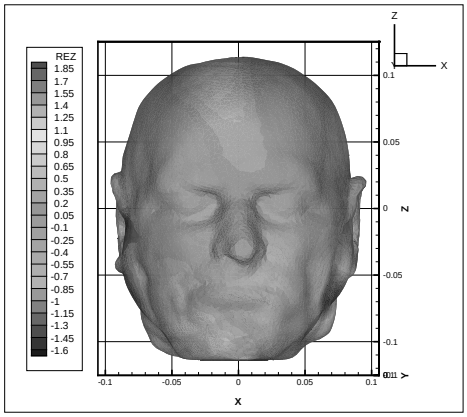

(d) method DG-$\mathbb{P}_0$-c, time-harmonic, skin, frontal view, mesh M2.

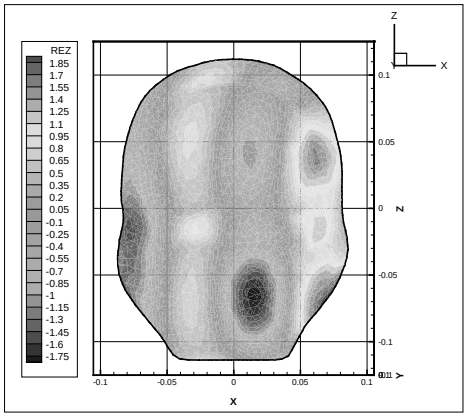

(e) method DG-$\mathbb{P}_1$-c, time-domain, view in the plane Y=0.0 m, mesh M1.

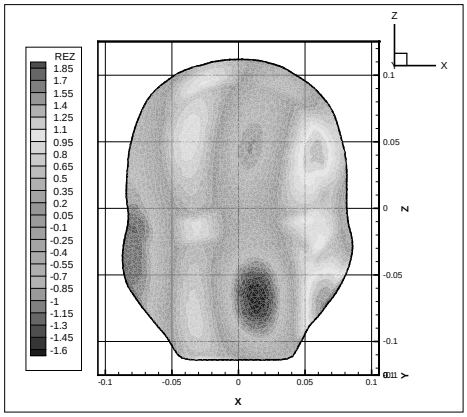

(f) method DG-$\mathbb{P}_0$-c, time-harmonic, view in the plane Y=0.0 m, mesh M2.

FIG. 10 – Propagation of a plane wave in a heterogeneous medium, F=1800 MHz. Contour lines of E_z.

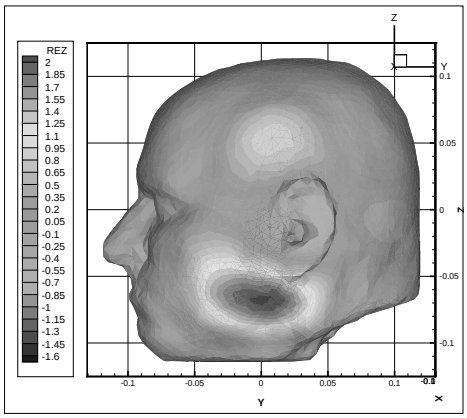

(a) method DG-$\mathbb{P}_1$-c, time-harmonic, skin, lateral view, mesh M1.

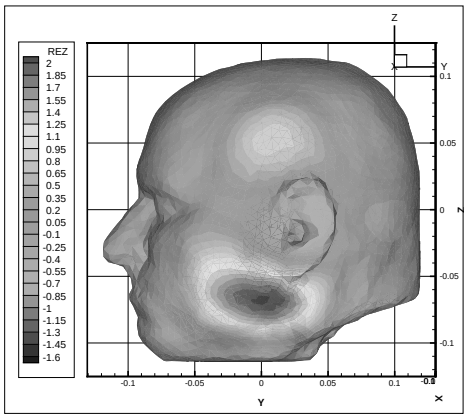

(b) method DG-$\mathbb{P}_1$-u, time-harmonic, skin, lateral view, mesh M1.

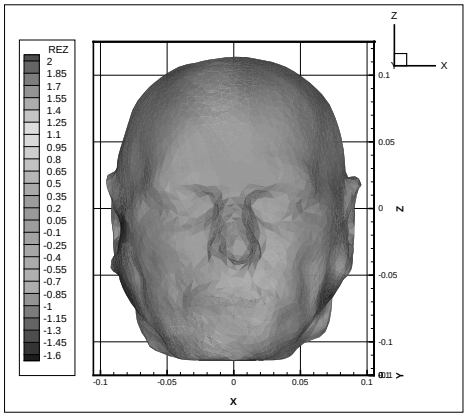

(c) method DG-$\mathbb{P}_1$-c, time-harmonic, skin, frontal view, mesh M1.

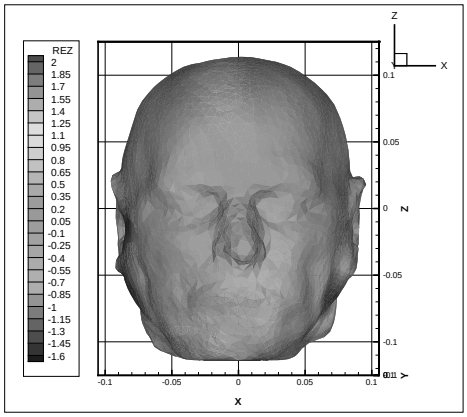

(d) method DG-$\mathbb{P}_1$-u, time-harmonic, skin, frontal view, mesh M1.

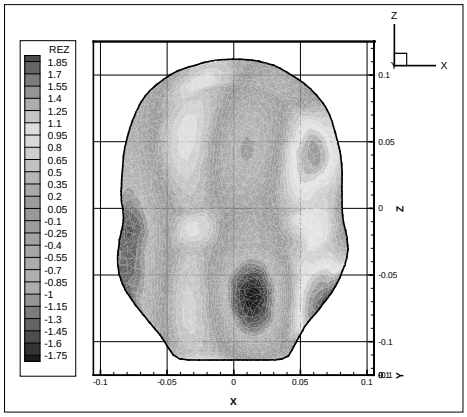

(e) method DG-$\mathbb{P}_1$-c, time-harmonic, view in the plane Y=0.0 m, mesh M1.

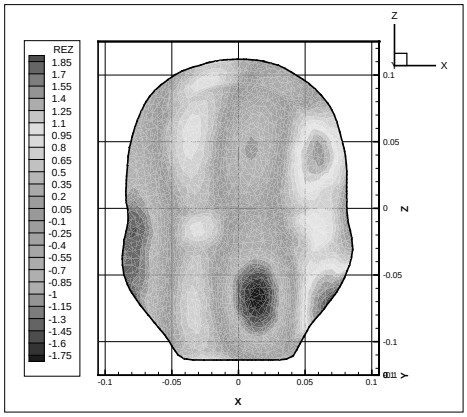

(f) method DG-$\mathbb{P}_1$-u, time-harmonic, view in the plane Y=0.0 m, mesh M1.

FIG. 11 – Propagation of a plane wave in a heterogeneous medium, F=1800 MHz. Contour lines of E_z.

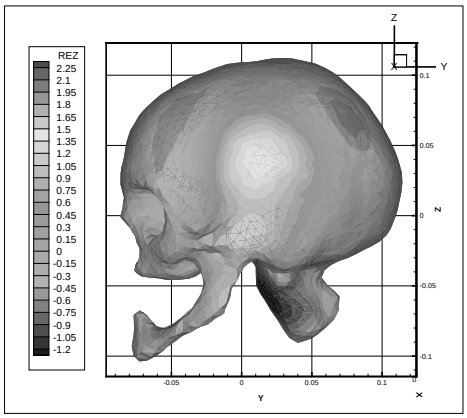

(a) method DG-$\mathbb{P}_1$-c, time-domain, skull, left side, mesh M1.

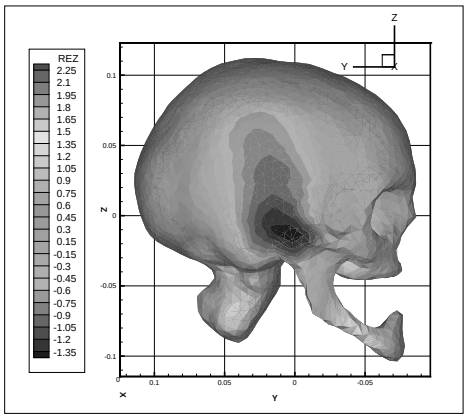

(b) method DG-$\mathbb{P}_1$-c, time-domain, skull, right side, mesh M1.

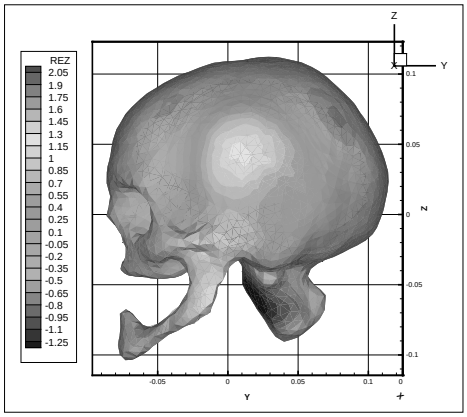

(c) method DG-$\mathbb{P}_1$-c, time-harmonic, skull, left side, mesh M1.

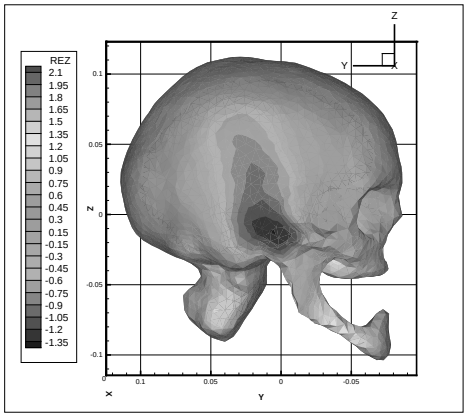

(d) method DG-$\mathbb{P}_1$-c, time-harmonic, skull, right side, mesh M1.

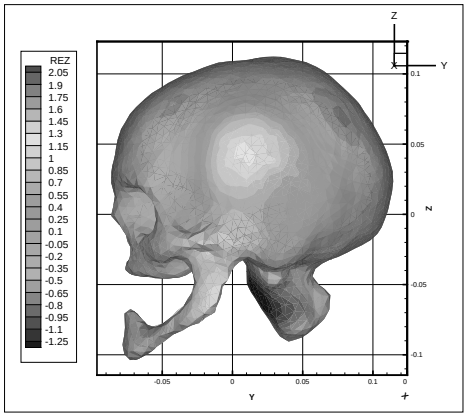

(e) method DG-$\mathbb{P}_1$-u, time-harmonic, skull, left side, mesh M1.

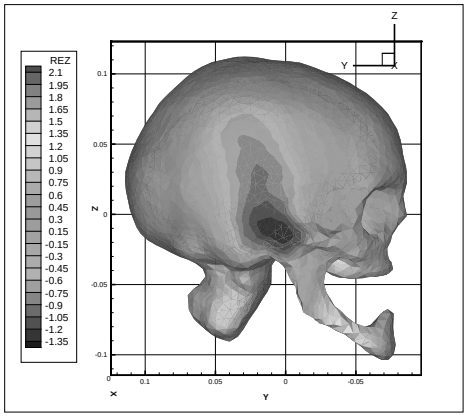

(f) method DG-$\mathbb{P}_1$-u, time-harmonic, skull, right side, mesh M1.

FIG. 12 – Propagation of a plane wave in a heterogeneous medium, F=1800 MHz. Contour lines of E_z.

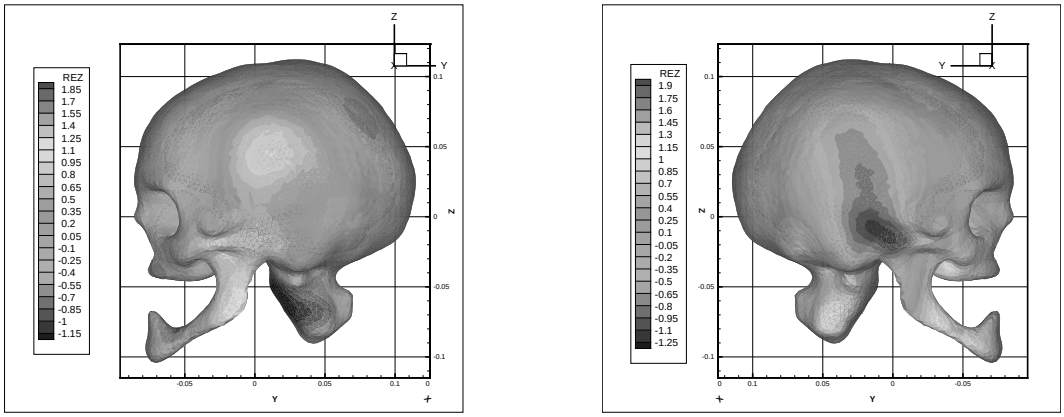

(a) Skull, left side.

(b) Skull, right side.

FIG. 13 – Propagation of a plane wave in a heterogeneous medium, F=1800 MHz. Contour lines of E_z : method DG-$\mathbb{P}_0$-c with mesh M2.

Références

[1] A. Alonso-Rodriguez and L. Gerardo-Giorda. New nonoverlapping domain decomposition methods for the harmonic Maxwell system. *SIAM J. Sci. Comput.*, 28(1) :102–122, 2006.

[2] P.R. Amestoy, I.S. Duff, and J.-Y. L'Excellent. Multifrontal parallel distributed symmetric and unsymmetric solvers. *Comput. Meth. App. Mech. Engng.*, 184 :501–520, 2000.

[3] M. Benzi, J.C. Haws, and M. Tuma. Preconditioning highly indefinite and nonsymmetric matrices. *SIAM J. Sci. Comput.*, 22(4) :1333–1353, 2000.

[4] P. Bernardi, M. Cavagnaro, S. Pisa, and E. Piuzzi. Specific absorption rate and temperature increases in the head of a cellular phone user. *IEEE Trans. Microwave Theory Tech.*, 48(7) :1118–1126, 2000.

[5] J.-D. Boissonnat and S. Oudot. Provably good sampling and meshing of surfaces. *Graphical Models*, 67(5) :405–451, 2005.

[6] F. Bourdel, P.A. Mazet, and P. Helluy. Resolution of the non-stationary or harmonic Maxwell equations by a discontinuous finite element method. In *10th International Conference in Computing Methods in Applied Sciences and Engineering*, pages 1–18, Paris, 1992. Nova Science.

[7] A. Buffa and I. Perugia. Discontinuous Galerkin approximation of the Maxwell eigenproblem. *SIAM J. Numer. Anal.*, 44(5) :2198–2226, 2006.

[8] L.P. Chew. Guaranteed-quality mesh generation for curved surfaces. In *9th Annual ACM Symposium Computational Geometry*, pages 274–280. ACM Press, 1993.

[9] P. Collino, G. Delbue, P. Joly, and A. Piacentini. A new interface condition in the non-overlapping domain decomposition. *Comput. Methods Appl. Mech. Engrg.*, 148 :195–207, 1997.

[10] B. Després. Décomposition de domaine et problème de Helmholtz. *C.R. Acad. Sci. Paris*, 1(6) :313–316, 1990.

[11] B. Després, P. Joly, and J.E. Roberts. A domain decomposition method for the harmonic Maxwell equations. In *Iterative methods in linear algebra*, pages 475–484, Amsterdam, 1992. North-Holland.

[12] V. Dolean, H. Fol, S. Lanteri, and R. Perrussel. Solution of the time-harmonic Maxwell equations using discontinuous Galerkin methods. *To appear in J. Comput. Appl. Math.*, 2007.

[13] V. Dolean, L. Gerardo-Giorda, and M. Gander. Optimized Schwarz methods for Maxwell equations, 2006. Submitted.

[14] M. Duruflé. *Intégration numérique et éléments finis d'ordre élevé appliqués aux équations de Maxwell en régime harmonique.* Thèse de doctorat en mathématiques Appliquées, Université Paris Dauphine, 2006.

[15] A. Ern and J.-L. Guermond. Discontinuous Galerkin methods for Friedrichs systems I. General theory. *SIAM J. Numer. Anal.*, 44(2) :753–778, 2006.

[16] A. Ern and J.-L. Guermond. Discontinuous Galerkin methods for Friedrichs systems II. Second-order elliptic PDE's. *SIAM J. Numer. Anal.*, 44(6) :2363–2388, 2006.

[17] L. Fezoui, S. Lanteri, S. Lohrengel, and S. Piperno. Convergence and stability of a discontinuous Galerkin time-domain method for the 3D heterogeneous Maxwell equations on unstructured meshes. *ESAIM : Math. Model. Numer. Anal.*, 39(6) :1149–1176, 2005.

[18] P. Frey. YAMS : a fully automatic adaptive isotropic surface remeshing procedure. INRIA Research Report No. 4252, 2003.

[19] P.-L. George, F. Hecht, and E. Saltel. Automatic mesh generator with specified boundary. *Comput. Methods Appl. Mech. Engrg.*, 92 :269–288, 1991.

[20] P. Helluy. *Résolution numérique des équations de Maxwell harmoniques par une méthode d'éléments finis discontinus.* Thèse en mathématiques appliquées, Ecole Nationale Supérieure de l'Aéronautique, 1994.

[21] P. Helluy and S. Dayma. Convergence d'une approximation discontinue des systèmes du premier ordre. *C. R. Acad. Sci. Paris Sér. I Math.*, 319(12) :1331–1335, 1994.

[22] P. Hénon, P. Ramet, and J. Roman. PaStiX : a high-performance parallel direct solver for sparse symmetric definite systems. *Parallel Comput.*, 28 :301–321, 2002.

[23] J.S. Hesthaven and T. Warburton. Nodal high-order methods on unstructured grids. I. Time-domain solution of Maxwell's equations. *J. Comput. Phys.*, 181(1) :186–221, 2002.

[24] P. Houston, I. Perugia, A. Schneebeli, and D. Schötzau. Interior penalty method for the indefinite time-harmonic Maxwell equations. *Numer. Math.*, 100(3) :485–518, 2005.

[25] P. Houston, I. Perugia, A. Schneebeli, and D. Schötzau. Mixed discontinuous Galerkin approximation of the Maxwell operator : the indefinite case. *ESAIM : Math. Model. Numer. Anal.*, 39(4) :727–753, 2005.

[26] G. Karypis and V. Kumar. A fast and high quality multilevel scheme for partitioning irregular graphs. *SIAM J. Sci. Comput.*, 20(1) :359–392, 1999.

[27] J. Kurzak and J. Dongarra. Implementation of the mixed-precision in solving systems of linear equations on the CELL processor. Technical Report UT-CS-06-580, University of Tennessee, 2006.

[28] J. Langou, J. Langou, P. Luszczek, J. Kurzak, A. Buttari, and J. Dongarra. Exploiting the performance of 32 bit floating point arithmetic in obtaining 64 bit accuracy. Technical Report UT-CS-06-574, University of Tennessee, 2006.

[29] W. Lorensen and H. Cline. Marching cubes : a high resolution 3D surface construction algorithm. In *Siggraph 87*, volume 21, pages 163–170, 1987.

[30] Peter Monk. *Finite element methods for Maxwell's equations.* Numerical Mathematics and Scientific Computation. Oxford University Press, New York, 2003.

[31] I. Perugia, D. Schötzau, and P. Monk. Stabilized interior penalty methods for the time-harmonic Maxwell equations. *Comput. Methods Appl. Mech. Engrg.*, 191(41-42) :4675–4697, 2002.

[32] S. Piperno. L^2-stability of the upwind first order finite volume scheme for the Maxwell equations in two and three dimensions on arbitrary unstructured meshes. *M2AN : Math. Model. Numer. Anal.*, 34(1) :139–158, 2000.

[33] P. Ratiu, B. Hillen, J. Glaser, and D. P. Jenkins. *Medicine Meets Virtual Reality 11 - NextMed : Health Horizon*, volume 11, chapter Visible Human 2.0 - the next generation, pages 275–281. IOS Press, 2003.

[34] Y. Saad and H. Schultz. GMRES : Generalized minimal residual algorithm for solving non-symmetric linear systems. *SIAM J. Sci. Stat. Comput.*, 7 :856–869, 1986.

[35] G.L.G. Sleijpen and D.R. Fokkema. BiCGstab(ℓ) for linear equations involving unsymmetric matrices with complex spectrum. *Electron. Trans. Numer. Anal.*, 1 :11–32 (electronic only), 1993.

Unité de recherche INRIA Sophia Antipolis
2004, route des Lucioles - BP 93 - 06902 Sophia Antipolis Cedex (France)

Unité de recherche INRIA Futurs : Parc Club Orsay Université - ZAC des Vignes
4, rue Jacques Monod - 91893 ORSAY Cedex (France)
Unité de recherche INRIA Lorraine : LORIA, Technopôle de Nancy-Brabois - Campus scientifique
615, rue du Jardin Botanique - BP 101 - 54602 Villers-lès-Nancy Cedex (France)
Unité de recherche INRIA Rennes : IRISA, Campus universitaire de Beaulieu - 35042 Rennes Cedex (France)
Unité de recherche INRIA Rhône-Alpes : 655, avenue de l'Europe - 38334 Montbonnot Saint-Ismier (France)
Unité de recherche INRIA Rocquencourt : Domaine de Voluceau - Rocquencourt - BP 105 - 78153 Le Chesnay Cedex (France)

Éditeur
INRIA - Domaine de Voluceau - Rocquencourt, BP 105 - 78153 Le Chesnay Cedex (France)
http://www.inria.fr
ISSN 0249-6399